

1 **Coherent streamflow variability in Monsoon Asia over**  
2 **the past eight centuries—links to oceanic drivers**

3 **Hung T.T. Nguyen<sup>1</sup>, Sean W.D. Turner<sup>2</sup>, Brendan M. Buckley<sup>3</sup>, and Stefano**  
4 **Galelli<sup>1</sup>**

5 <sup>1</sup>Pillar of Engineering Systems and Design, Singapore University of Technology and Design, Singapore

6 <sup>2</sup>Pacific Northwest National Laboratory, Washington, USA

7 <sup>3</sup>Lamont-Doherty Earth Observatory, Columbia University, New York, USA

8 **Key Points:**

- 9 • Climate-informed dynamic streamflow reconstruction is skillful over most of Mon-  
10 soon Asia
- 11 • Streamflow in Monsoon Asia is spatially coherent
- 12 • Reconstruction reveals spatial and temporal variability in streamflow–ocean tele-  
13 connections

---

Corresponding author: Hung Nguyen, [tanthaihung\\_nguyen@mymail.sutd.edu.sg](mailto:tanthaihung_nguyen@mymail.sutd.edu.sg)

**Abstract**

The Monsoon Asia region is home to ten of the world's biggest rivers, supporting the lives of 1.7 billion people who rely on streamflow for water, energy, and food. Yet, a synoptic understanding of multi-centennial streamflow variability for this region is lacking. To fill this gap, we produce the first large scale streamflow reconstruction over Monsoon Asia (62 stations in 16 countries, 813 years of mean annual flow). In making this reconstruction, we develop a novel, automated, climate-informed, and dynamic reconstruction framework that is skillful over most of the region. We show that streamflow in Monsoon Asia is spatially coherent, owing to common drivers from the Pacific, Indian, and Atlantic Oceans. We also show how these oceanic teleconnections change over space and time. By characterizing past and present hydroclimatic variability, we provide a platform for assessing the impact of future climatic changes and informing water management decisions.

**Plain Language Summary**

Ten of the world's biggest rivers are located entirely within the Asian Monsoon region. They provide water, energy, and food for 1.7 billion people. To manage these critical resources, we need a better understanding of river discharge—how does it change over a long time? Are there common variation patterns among rivers? To answer these questions, we use information derived from tree rings to reconstruct average annual river discharge history at 62 gauges in 16 Asian countries. Our reconstruction reveals the riparian footprint of megadroughts and large volcanic eruptions over the past eight centuries. We show that simultaneous droughts and pluvials have often occurred at adjacent river basins in the past, because Asian rivers share common influences from the Pacific, Indian, and Atlantic Oceans. We also show how these oceanic teleconnections change over space and time. Our findings can inform big decisions made on water-dependent infrastructure, thus benefiting the riparian people of the Asian Monsoon region.

## 1 Introduction

Of the world’s 30 biggest rivers, ten are located within Monsoon Asia, and two others originate from this region (Figure 1). These river basins are home to 1.7 billion people (Best, 2019). With high population densities, even smaller basins support the livelihood of millions—e.g., Chao Phraya (Thailand): 25 million, Angat (the Philippines): 13 million, and Citarum (Indonesia): 10 million (Nguyen & Galelli, 2018; Libisch-Lehner et al., 2019; D’Arrigo et al., 2011). River discharge, or *streamflow*, provides water for domestic and industrial uses, irrigation, and hydropower. It sustains aquatic life (including fish yield), carries sediment and nutrients, and helps prevent salinization of river deltas. Streamflow is an important link in both the water-energy-food nexus and the ecological cycle. To manage this resource, we need a good understanding of hydrologic variability. Such understanding is often derived from streamflow measurements; however, these instrumental data span typically only a few decades, too short to capture long-term variability and changes in streamflow.

When compared against instrumental data, longer streamflow records reconstructed from climate proxies—such as tree rings—often reveal striking insights. A reconstructed pre-dam variability of the Yellow River (Li et al., 2019) shows that streamflow in 1968–2010 was only half of what should have been; in other words, human withdrawals for agriculture, industry, and municipalities reduced streamflow by half! A reconstruction of the Citarum River (Indonesia) (D’Arrigo et al., 2011) shows that the period 1963–2006 contained an increasing trend of low flow years but no trend in high flow years, compared with the previous three centuries. This finding suggests that 10 million inhabitants of Jakarta may be facing higher drought risks than what is perceived from the instrumental record. The Mongolian “Breadbasket”, an agricultural region in north-central Mongolia (Pederson et al., 2013), experienced an unusually wet twentieth-century, and the recent dry epoch is not rare in the last four centuries (Davi et al., 2006; Pederson et al., 2013; Davi et al., 2013). Consequently, agricultural planning cannot take the twentieth century to be the norm, lest history repeats the lesson of the Colorado River Basin: observations over abnormally wet years (Stockton & Jacoby, 1976; Woodhouse et al., 2006; Robeson et al., 2020) led to water rights over-allocation, and the Colorado no longer reaches the Pacific Ocean.

The case of the Colorado River demonstrates that streamflow reconstructions can improve our understanding of water resources availability. Furthermore, with longer streamflow records, low frequency variations of streamflow can be revealed, the frequency and magnitude of floods and droughts can be better quantified, and the risks associated with these natural disasters can be better assessed—these benefits have been demonstrated in Australia (Allen et al., 2017; Tozer et al., 2018), the United States (DeRose et al., 2015; Stagge et al., 2018), Canada (Hart et al., 2010; Sauchyn et al., 2015) and other countries (Lara et al., 2015; Güner et al., 2017). Streamflow reconstructions have also been used to generate stochastic time series for water management applications (Prairie et al., 2008; Sauchyn & Ilich, 2017). These benefits, if realized in Monsoon Asia, can improve the lives of many people, given the dense populations of river basins in this region.

82 Compelling evidence calls for more streamflow reconstructions in Monsoon Asia.  
83 Tremendous efforts, particularly in the last four years (Figure S1), have partly addressed  
84 this need, but the hydrological knowledge gained was limited to individual catchments,  
85 more than half of which are in China (Figure S1 and Table S1). A synoptic understand-  
86 ing is lacking. Here, we produce the first large-scale streamflow reconstruction for Mon-  
87 soon Asia, covering 62 stations in 16 countries, unraveling eight centuries of annual stream-  
88 flow variability. To achieve this task, we develop a novel automated framework with three  
89 main components: (1) a climate-informed proxy selection procedure, (2) a dynamic state-  
90 space reconstruction model, and (3) a rigorous cross-validation routine for parameter tun-  
91 ing to achieve optimal skills. We also use the Monsoon Asia Drought Atlas version 2 as  
92 the paleoclimatic proxy instead of a tree ring network, as the former offers computational  
93 advantages (supported with strong physical and statistical foundations) for this large-  
94 scale reconstruction. With this work, 58 stations are reconstructed for the first time while  
95 the other four (Citarum, Yerru, Ping, and Indus Rivers) are extended back in time com-  
96 pared to previous works (D’Arrigo et al., 2011; Pederson et al., 2013; Nguyen & Galelli,  
97 2018; Rao et al., 2018). This data set allows us to assess both local historical water avail-  
98 ability and regional streamflow patterns, revealing the spatial coherence of streamflow  
99 and its links to the oceans. This understanding may improve the management of river  
100 basins and other water-dependent resources.

## 101 2 Data

### 102 2.1 Streamflow Data

103 Our reconstruction target is the mean annual flow, and we used the calendar year  
104 (January to December) as there is not a common water year across Monsoon Asia (Knoben  
105 et al., 2018). We obtained streamflow data from the Global Streamflow Indices and Meta-  
106 data Archive (GSIM) (Do et al., 2018; Gudmundsson et al., 2018), using stations hav-  
107 ing at least 41 years of data, and with less than 3% missing daily values. We also received  
108 streamflow data from our colleagues for some countries where public streamflow records  
109 are not available (see Acknowledgment). Small catchments may be influenced by local  
110 conditions more than by broad climate inputs that are captured in the regional paleo-  
111 climate proxies (Strange et al., 2019). Therefore, we used only stations where the mean  
112 annual flow over the whole time series is at least  $50 \text{ m}^3/\text{s}$ ; this threshold is heuristic, and  
113 somewhat arbitrary. Details of this initial selection step are provided in Text S2 and in  
114 the code repository for this paper ([ntthung.github.com/paleo-asia](https://ntthung.github.com/paleo-asia), DOI: 10.5281/  
115 [zenodo.3818117](https://doi.org/10.5281/zenodo.3818117).)

116 Many stations in our collection have upstream reservoirs that may interfere with  
117 the proxy-streamflow relationship. This interference is stronger for seasonal streamflow  
118 than annual streamflow: reservoirs transfer water from the wet season to the dry sea-  
119 son, but not all reservoirs retain water from year to year. Reservoirs that are filled and  
120 emptied within a year do not change the annual water budget downstream. To minimize  
121 reservoir interference, we reconstructed annual streamflow, and we removed stations that  
122 have upstream retention times longer than a year. We identified upstream reservoirs by

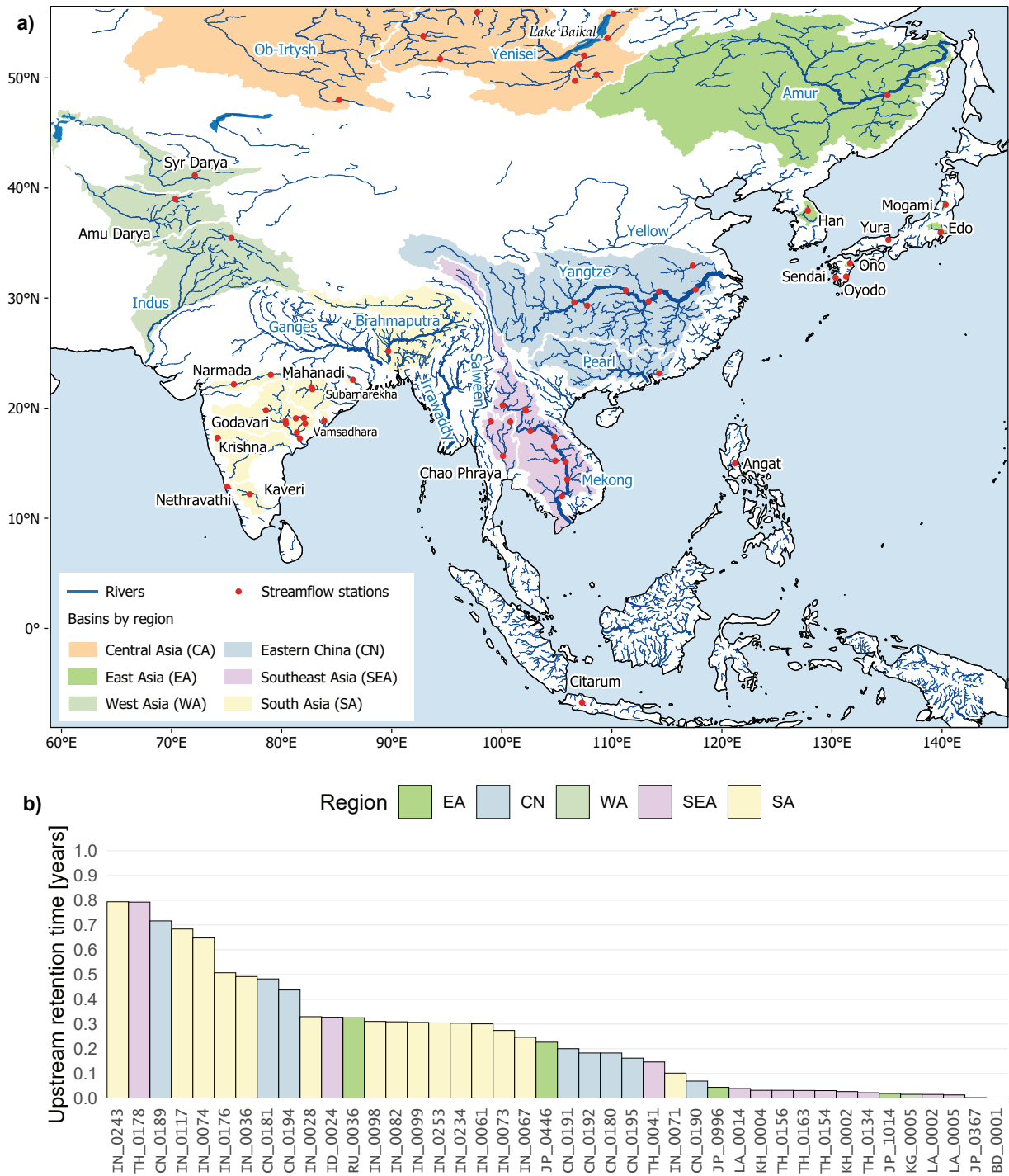


**Figure 1.** a) The Monsoon Asia region (Cook et al., 2010); river basins involved in this study are highlighted by sub-region, rivers belonging to the world’s 30 biggest (Best, 2019) shown with blue names. b) Upstream retention time of the 42 stations that have upstream reservoirs. The bar colours denote the regions according to a). The first two letters of each station’s code indicates the country it is in. Refer to Table S2 for station details.

123 overlaying the Global Reservoirs and Dams (GRanD) data (Lehner et al., 2011) on the  
124 river network (Lehner & Grill, 2013; Barbarossa et al., 2018). The upstream retention  
125 time was calculated as the total upstream reservoir capacity (million m<sup>3</sup>) divided by the  
126 mean annual flow volume (million m<sup>3</sup>/year). For stations having over-year reservoirs con-  
127 structed towards the end of their records, we also truncated the corresponding years, keep-  
128 ing only the streamflow data before dam construction.

129 Our collection and quality control effort resulted in an annual streamflow data set  
130 of 62 stations in 16 countries. Our records span across Monsoon Asia, covering the fol-  
131 lowing sub-regions: Central Asia (CA), East Asia (EA), eastern China (CN), West Asia  
132 (WA), Southeast Asia (SEA), and South Asia (SA). The stations' locations and upstream  
133 retention times (for those having upstream reservoirs) are shown in Figure 1.

## 134 2.2 Proxy Data

135 Our paleoclimate proxy is the Monsoon Asia Drought Atlas version 2 (MADA v2)  
136 (Cook, 2015), built upon the original MADA of Cook et al. (2010). The MADA is a grid-  
137 ded data set of the Palmer Drought Severity Index (PDSI) (W. C. Palmer, 1965) over  
138 the Asian monsoon region; each grid cell contains an annual time series of the mean June-  
139 July-August PDSI, reconstructed from tree rings, and calibrated with the instrumental  
140 data set of Dai et al. (2004). The MADA proves to be a reliable long-term record of mon-  
141 soon strength, having revealed the spatiotemporal extents of the four Asian megadroughts  
142 in the last millennium, and linking variations in monsoon strength to sea surface tem-  
143 perature patterns. MADA v2 improves over its predecessor by incorporating more tree  
144 ring chronologies (453 versus 327), and targeting the self-calibrating PDSI (scPDSI), which  
145 addresses several limitations of the standard PDSI (Wells et al., 2004; van der Schrier  
146 et al., 2013). We use the MADA v2 portion between 1200–2012 as this is the common  
147 period of most grid points in the atlas (Figure S4), and is also the stable portion with  
148 sufficient number of tree ring chronologies in the source tree ring network.

149 Drought atlases reconstructed from tree rings have been shown to be practical pa-  
150 leoclimate proxies for streamflow reconstruction. Earlier experiments used individual grid  
151 points to reconstruct streamflow, either in combination with ring widths (Coulthard et  
152 al., 2016) or on their own (Graham & Hughes, 2007; Adams et al., 2015). Ho et al. (2016,  
153 2017), and Nguyen and Galelli (2018) then formalized the methodology and provided the-  
154 oretical considerations. They reasoned that since both streamflow and PDSI can be mod-  
155 eled as functions of ring width, one can also build a model to relate streamflow to PDSI.  
156 Moreover, drought atlases enhance the spatial expression of the underlying tree ring data—  
157 by incorporating the modern PDSI field in its calibration—and are also more uniform  
158 in space and time than the tree ring network itself (see Cook et al., 2010, Figure 1), mak-  
159 ing them better suited to large-scale studies. We now elaborate these points as we de-  
160 scribe the reconstruction framework.

### 3 Reconstruction Framework

#### 3.1 Using a Drought Atlas as Paleoclimate Proxy

##### 3.1.1 Physical basis

The main physical processes that involve climate and tree growth are depicted in Figure 2a. The climate at a given location can be characterized by precipitation and temperature, among others. These climatic inputs control soil moisture on land. Except for losses (such as groundwater recharge, evaporation, and surface runoff), the net soil moisture storage then follows two main paths: one goes out of the catchment as streamflow, the other is taken up by the trees and transpired back into the atmosphere, influencing tree growth along the way. Thus, tree growth and streamflow are connected via land-atmosphere interactions—this is the basis for streamflow reconstruction from tree rings (cf. Rao et al., 2018; Li et al., 2019). Note, however, that tree growth does not directly control streamflow, and neither does streamflow control tree growth; we can infer a relationship between them only because they are both influenced by soil moisture. On the other hand, soil moisture directly controls streamflow and is, in principle, a reasonable predictor for streamflow.

It would thus be ideal to have a “natural” soil moisture proxy record, but of course that is not the case. We can instead rely on a surrogate—a soil moisture record reconstructed from tree rings, such as the MADA.

##### 3.1.2 Statistical basis

The physical discussion above yields three types of paleoclimate reconstruction: streamflow from tree rings, soil moisture from streamflow, and streamflow from soil moisture. We now derive mathematically the relationships between these reconstruction types.

Each reconstruction is a conditional distribution of one variable (e.g. streamflow) given that we have observed another variable (e.g. soil moisture), and given the historical climate. We represent these conditional distributions with a probabilistic graphical model (Koller & Friedman, 2009) as shown in Figure 2b. There are four random variables involved: climate ( $C$ ), soil moisture ( $S$ ), ring width ( $R$ ), and streamflow ( $Q$ ). Each of these variables can be multivariate, i.e.,  $C$  includes precipitation and temperature, among others, and all variables can include multiple sites or grid points. As a convention, let  $f_X(x)$  be the probability density function (PDF) of the random variable  $X$ ,  $f_{XY}(x, y)$  be the joint PDF of  $X$  and  $Y$ , and  $f_{X|Y}(x|y)$  be the conditional PDF of  $X$  given that  $Y = y$ .

Reconstructing streamflow from tree rings is essentially deriving the distribution of  $Q$  given  $R$  and  $C$ , i.e.  $f_{Q|R,C}(q|r, c)$ , where  $r$  is the measured ring width index, and  $c$  is the historical climate. We can decompose this distribution as follows:

$$\begin{aligned} f_{Q|R,C}(q|r, c) &= \int f_{Q,S|R,C}(q, s|r, c) ds \\ &= \int f_{Q|S,R,C}(q|s, r, c) f_{S|R,C}(s|r, c) ds. \end{aligned} \tag{1}$$

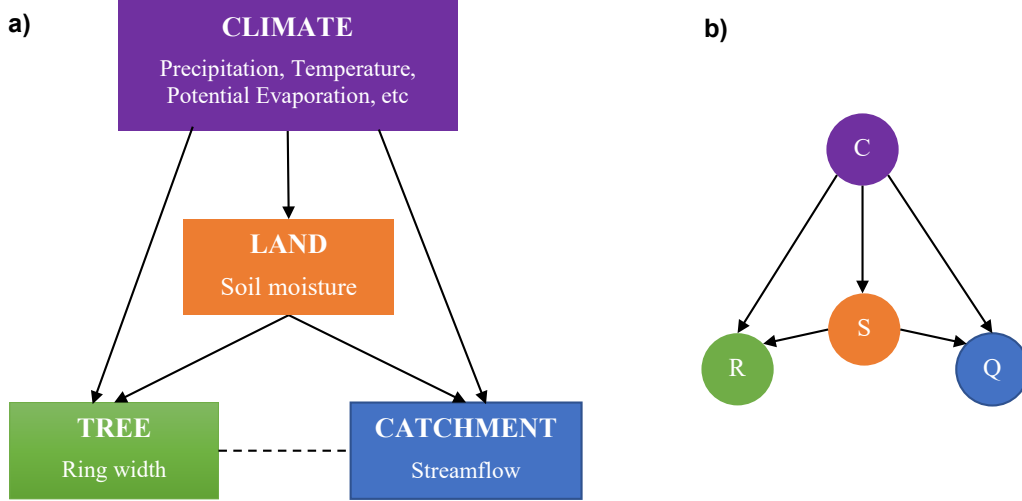


**Figure 2.** a) Relationships between hydroclimatic variables and tree growth. b) A probabilistic graphical model representing the relationships in a), where  $C$  is a vector of climate variables,  $S$  the soil moisture,  $R$  the ring width index, and  $Q$  streamflow. The arrows represent the conditional dependence among variables.

198 The first equality comes from the relationship between marginal and joint distributions.  
 199 The second equality comes from Bayes' theorem. Now,  $Q$  is independent of  $R$  given  $S$   
 200 and  $C$  (Figure 2b), so  $f_{Q|S,R,C}(q|r,c) = f_{Q|S,C}(q|s,c)$ . Consequently,

$$201 \quad f_{Q|R,C}(q|r,c) = \int f_{Q|S,C}(q|s,c) f_{S|R,C}(s|r,c) ds. \quad (2)$$

202 Observe that  $f_{Q|S,C}$  is the streamflow reconstruction from the MADA, and  $f_{S|R,C}$   
 203 is the MADA reconstruction from tree rings. Thus we have established mathematically  
 204 the reasoning that tree-ring-based streamflow reconstruction is possible based on the link  
 205 through soil moisture.  $f_{Q|R,C}$  is the marginal distribution without observing the soil mois-  
 206 ture. Instead of constructing  $f_{Q|R,C}$ , we can infer  $S$  from  $R$ , then  $Q$  from  $S$ , by construct-  
 207 ing  $f_{S|R,C}$  and  $f_{Q|S,C}$ .

### 208 **3.1.3 Computational advantages of using the MADA, and caveats**

209 The MADA can be thought of as a transformation from the tree ring network, ir-  
 210 regular in both space and time, to a regular grid with homogeneous temporal coverage—  
 211 analogous to transforming meteorological station data to gridded temperature and pre-  
 212 cipitation products. This transformation brings several advantages to reconstructing stream-  
 213 flow using the MADA, compared to using the underlying tree ring network.

214 First, in a typical reconstruction study, one must detrend and standardize the tree  
 215 ring data to remove non-climate signals (cf. Cook & Kairiukstis, 1990). For a large scale  
 216 study like ours, such a task is complex. Instead, we can leverage the effort that has been

217 devoted to detrending and standardizing the chronologies in making the MADA, and use  
218 the MADA as proxy, having built the physical and statistical foundations to do so.

219 Second, the tree ring sites often cluster, with vast empty space between clusters  
220 (see e.g. Cook et al. (2010), Figure 1). When taking a subset of them for reconstruction  
221 at a station, there can be cases where none or very few sites are within a search radius.  
222 The MADA helps “bridging” the space, bringing climate signals from further-away tree  
223 sites to grid points nearer to the station. The high resolution grid ( $1^\circ \times 1^\circ$  for version  
224 2) makes automated grid point selection easier. (The automated grid point selection pro-  
225 cedure is described in Section 3.2.1.)

226 Third, when reconstructing streamflow from tree rings, nested models are often nec-  
227 essary because tree ring chronologies have different time spans. One starts with the short-  
228 est nest, using the common time span of all chronologies to build a model, then drop-  
229 ping the shortest chronology to build a second model with longer time span but less ex-  
230 plained variance than the first, and repeating the process, dropping more chronologies  
231 to achieve longer time spans until the final nest with the longest time span, but with the  
232 lowest explained variance. The nests’ outputs are then corrected for their variance and  
233 averaged to obtain the final reconstruction (see e.g. D’Arrigo et al., 2011). This nest-  
234 ing step was carried out for the MADA, such that most grid points have the same time  
235 span (Figure S4). This lets us use a single common period (1200-2012), and eliminates  
236 our need to build nested models back in time. This is particularly desirable for our dy-  
237 namic state-space reconstruction model, as averaging the nests breaks the link between  
238 the catchment state and streamflow. (The reconstruction model is described in Section  
239 3.2.2.)

240 The computational advantages of using the MADA are thus threefold: (1) no de-  
241 trending and standardization, (2) easier grid point selection, and (3) no nesting. How-  
242 ever, these come with some costs, the most important of which is uncertainty. When re-  
243 constructing streamflow from the MADA, we treat the MADA (i.e., the model input)  
244 as constant. But in fact, the MADA is a regression product and has its own uncertainty.  
245 One way to quantify this uncertainty is by bootstrapping: streamflow reconstructions  
246 can be built using bootstrap replicates of the MADA, and the range of the bootstrap en-  
247 semble indicates the uncertainty of the reconstruction. An appropriate bootstrapping  
248 scheme must be considered, given that dimensionality is the main challenge: the MADA  
249 has  $813 \text{ years} \times 2716 \text{ grid points}$ . The flip side is that the reconstruction framework runs  
250 for each station individually (see Section 3.2), so one need not reconstruct the whole net-  
251 work in order to quantify uncertainties at some stations of interest.

252 As a gridded regression product, the MADA may also smooth out local variabil-  
253 ities. This can be alleviated by carefully selecting and processing the grid points to re-  
254 tain as much variance as possible (Section 3.2.1), and by using sufficiently large catch-  
255 ments (Section 2.1).

256 Finally, we note that the computational advantages we described here are only ap-  
257 plicable to large-scale studies, where an automated framework is needed. For individ-

258 ual sites, we urge researchers to consider all available proxies, rather than being attracted  
 259 by the convenience offered by the drought atlases.

### 260 **3.2 Point-by-Point, Climate-informed, Dynamic Streamflow Reconstruc-** 261 **tion**

262 When reconstructing a climate field, such as a PDSI grid or a streamflow station  
 263 network, it is desirable to preserve the field covariance structure. However, building a  
 264 large-scale spatial regression model is challenging. Instead, one can reconstruct each point  
 265 in the field independently, and rely on the proxy network to capture the spatial patterns.  
 266 This is the premise of the Point-by-Point Regression (PPR) method (Cook et al., 1999),  
 267 which has been used to reconstruct drought atlases of Europe (Cook et al., 2015, 2020),  
 268 the Americas (Cook et al., 1999; Stahle et al., 2016; Morales et al., 2020), Oceania (J. G. Palmer  
 269 et al., 2015), and Asia (Cook et al., 2010). These drought atlases demonstrate that PPR  
 270 captures well the spatial patterns of climate variability (see e.g. Cook et al. (1999), Fig-  
 271 ures 8 and 9). Like these drought atlases, our streamflow network covers a large spatial  
 272 domain with varying climates; therefore, we adopted the PPR principle, and reconstructed  
 273 our stations individually. While some aspects of our reconstruction framework followed  
 274 the PPR procedure, we have innovated many steps of the workflow.

275 In a nutshell, the framework involves three main stages: (1) input selection (Sec-  
 276 tion 3.2.1), (2) model calibration (Section 3.2.2), and (3) cross-validation (Section 3.2.3).  
 277 In Stage 1, we selected a subregion of the MADA that is hydroclimatically similar to the  
 278 streamflow station of interest, and extracted from this subregion a parsimonious subset  
 279 of principal components, using weighted Principal Component Analysis (PCA). This stage  
 280 involves two tuning parameters: the hydroclimate similarity threshold, and the PCA weight.  
 281 For each combination of these parameters, we calibrated a reconstruction model in Stage  
 282 2, thus producing an ensemble of models. Finally, in Stage 3, we cross-validated the mod-  
 283 els to choose the best one, and used that for the final reconstruction.

#### 284 **3.2.1 Climate-informed Input Selection**

285 A regional paleoclimate proxy record, such as the MADA or its underlying tree ring  
 286 network, is rich with information, but not all of such information is relevant to the stream-  
 287 flow target. A proper input selection is necessary to filter noise and retain only the most  
 288 relevant signal. A common way is to use proxy sites within a search radius; and PPR  
 289 does the same. But, given that geographical proximity does not necessarily imply hy-  
 290 droclimatic similarity, we selected our proxies (MADA grid points) by hydroclimatic sim-  
 291 ilarity directly. The hydroclimate at location  $i$  (a MADA grid point or a streamflow sta-  
 292 tion) is characterized by three indices: aridity  $a_i$ , moisture seasonality  $s_i$ , and snow frac-  
 293 tion  $f_i$ , following Knoben, Woods, and Freer, who proposed this hydroclimate charac-  
 294 terization and calculated the indices for a global  $0.5^\circ \times 0.5^\circ$  grid (Knoben et al., 2018).  
 295 The hydroclimatic similarity between two locations  $i$  and  $j$  is then defined as their Eu-  
 296 clidean distance in the hydroclimate space. This distance is termed the KWF distance

297 and its mathematical definition is

$$298 \quad d_{KWF}(i, j) = \sqrt{(a_i - a_j)^2 + (s_i - s_j)^2 + (f_i - f_j)^2}. \quad (3)$$

299 By calculating the KWF distance between each MADA grid point and each stream-  
 300 flow station, we can screen out MADA grid points that are geographically close to the  
 301 station of interest but hydroclimatically different—a climate-informed grid point selec-  
 302 tion scheme. Whereas previous PPR implementations varied the search radius, we fixed  
 303 the radius to 2,500 km—the scale of regional weather systems (Boers et al., 2019)—and  
 304 varied the KWF distance between 0.1 and 0.3 in 0.05 increments. For reference, the max-  
 305 imum KWF distance between any two points in Monsoon Asia is 1.424. Each KWF dis-  
 306 tance yielded a search region encompassing a set of MADA grid points surrounding the  
 307 streamflow station of interest. In our search regions, PDSI often correlates significantly  
 308 and positively with streamflow (Figure 3); indeed hydroclimatic similarity is a physical  
 309 basis for correlation.

310 Next, we performed weighted PCA to remove multicollinearity among the MADA  
 311 grid points. Following PPR, we weighted each grid point by its correlation with the tar-  
 312 get streamflow, using equation (4):

$$313 \quad z_i = g_i r_i^p. \quad (4)$$

314 Here,  $g_i$  is grid point  $i$ 's scPDSI time series,  $r_i$  the correlation between  $g_i$  and the tar-  
 315 get streamflow,  $p$  the weight exponent, and  $z_i$  the weighted version of  $g_i$ . We used  $p =$   
 316  $0, 0.5, 2/3, 1, 1.5,$  and  $2$ , the same as those used by Cook et al. (2010). We then performed  
 317 PCA on  $z_i$ 's, and retained only those principal components (PCs) having eigenvalue at  
 318 least 1.0 (Hidalgo et al., 2000). From the retained PCs (typically about 20–40 per sta-  
 319 tion), we selected a parsimonious subset that is most relevant to the streamflow target  
 320 using the VSURF (Variable Selection Using Random Forest) algorithm (Genuer et al.,  
 321 2010). So, for each combination of KWF distance and PCA weight, we arrived at a sub-  
 322 set of PCs for reconstruction. Each streamflow station has an ensemble of 30 such sub-  
 323 sets, the best of which was identified using cross-validation (Section 3.2.3) and used for  
 324 the final reconstruction.

### 325 **3.2.2 Linear Dynamical System**

326 Having obtained the climatic inputs, the next step was to model the relationship  
 327 between these inputs and the catchment output (streamflow). Here, this relationship was  
 328 not modeled with linear regression (as with original PPR, and as typical with previous  
 329 reconstruction studies), but as a linear dynamical system (LDS), following equations (5)  
 330 and (6):

$$331 \quad x_{t+1} = Ax_t + Bu_t + w_t \quad (5)$$

$$332 \quad y_t = Cx_t + Du_t + v_t \quad (6)$$

333 where  $t$  is the time step (year),  $y$  the catchment output (streamflow),  $u$  the climatic in-  
 334 put (an ensemble member from the climate-informed grid point selection),  $w$  and  $v$  white  
 335 noise, and  $x$  the hidden system state, which can be interpreted as the catchment's flow

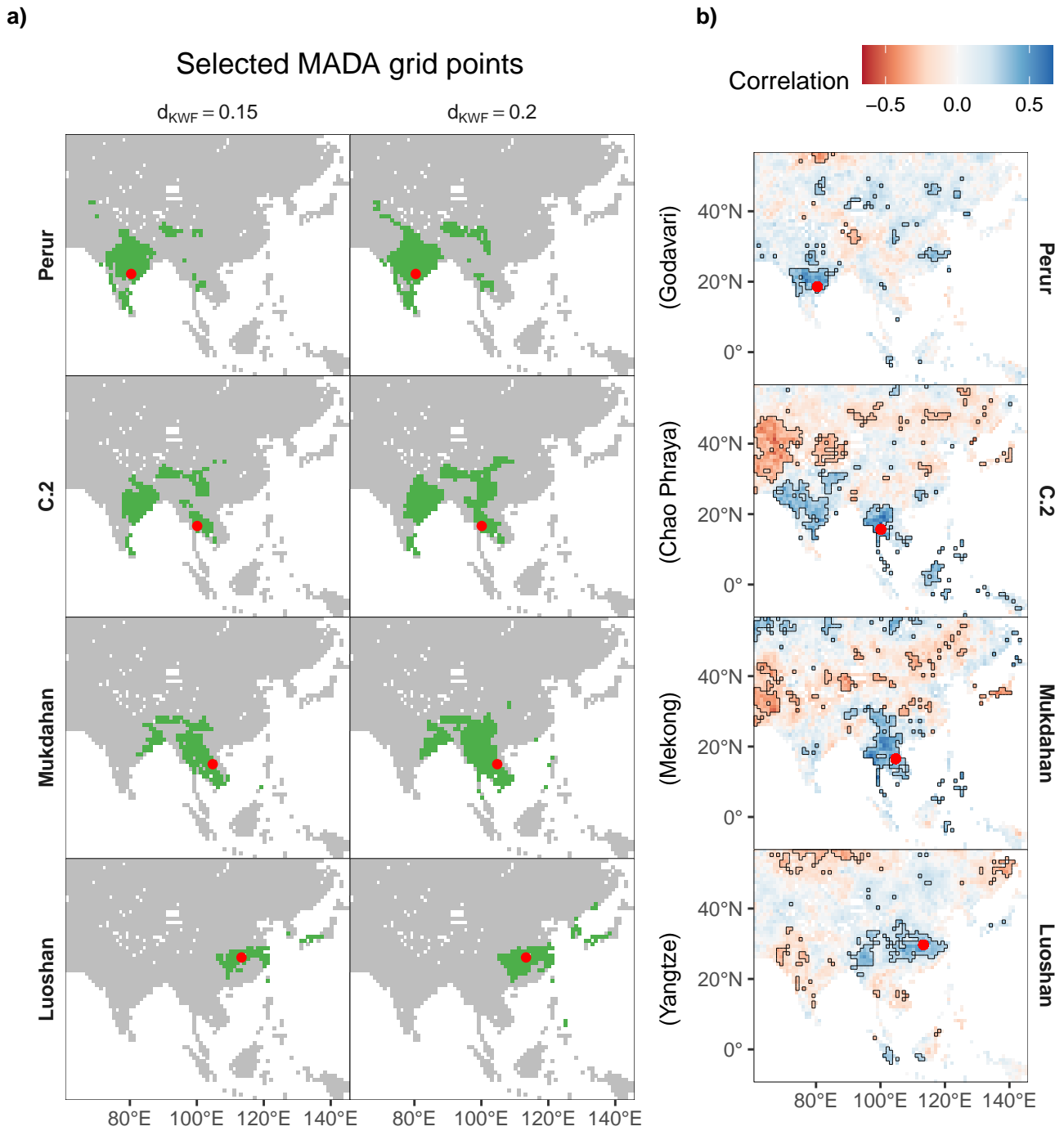


**Figure 3.** a) Examples of the climate-informed grid point selection: selected MADA grid points (green) based on two KWF distances (columns) at four stations (rows). b) Correlations between streamflow at the same four stations and the MADA, significant correlations ( $\alpha = 0.05$ ) enclosed in black boundaries. The selection regions in (a) generally have significant positive correlation with streamflow. The areas with significant negative correlations need further investigation.

336 regime, i.e. wet or dry (Nguyen & Galelli, 2018). By modeling the flow regime and its  
 337 transition, the LDS model accounts for both regime shifts (Turner & Galelli, 2016) and  
 338 catchment memory (Pelletier & Turcotte, 1997). These behaviors are not modeled in lin-  
 339 ear regression.

340 The LDS model assumes that the initial state and the noise processes are normally  
 341 distributed:

$$342 \quad w_t \sim \mathcal{N}(0, Q) \quad (7)$$

$$343 \quad v_t \sim \mathcal{N}(0, R) \quad (8)$$

$$344 \quad x_1 \sim \mathcal{N}(\mu_1, V_1). \quad (9)$$

345 It follows that the catchment state and output are also normally distributed. But some  
 346 of our streamflow records are skewed. These were log-transformed to reduce skewness  
 347 (Text S3 and Figure S3).

348 The LDS model is trained using a variant of the Expectation-Maximization algo-  
 349 rithm. In the E-step, we fix the model parameters and learn the hidden state. In the M-  
 350 step, we fix the hidden state and learn the model parameters. Iterations are repeated  
 351 between the E- and M-steps until convergence. The reconstruction algorithm is imple-  
 352 mented in the R package *lds* (Nguyen, 2020).

### 353 **3.2.3 Cross-validation**

354 Consistent with the literature, we assessed reconstruction performance using the  
 355 metrics Reduction of Error (RE) and Nash-Sutcliffe Coefficient of Efficiency (CE or NSE)  
 356 (Nash & Sutcliffe, 1970; Fritts, 1976). Mathematically,

$$357 \quad RE = 1 - \frac{\sum_{t \in \mathcal{V}} (Q_t - \hat{Q}_t)^2}{\sum_{t \in \mathcal{V}} (Q_t - \bar{Q}_c)^2} \quad (10)$$

$$358 \quad CE = 1 - \frac{\sum_{t \in \mathcal{V}} (Q_t - \hat{Q}_t)^2}{\sum_{t \in \mathcal{V}} (Q_t - \bar{Q}_v)^2} \quad (11)$$

359 where  $t$  is the time step,  $\mathcal{V}$  the validation set,  $Q$  the observed streamflow,  $\hat{Q}$  the recon-  
 360 structed streamflow,  $\bar{Q}_c$  the calibration period mean, and  $\bar{Q}_v$  the verification period mean.

361 Both RE and CE are based on squared error; they can be sensitive to outliers, es-  
 362 pecially the CE. To address this limitation, Gupta et al. (2009) proposed another met-  
 363 ric, which assesses a model output based on its correlation with observation, as well as  
 364 its bias and variability (equation (12)):

$$365 \quad KGE = 1 - \sqrt{(\rho - 1)^2 + \left(\frac{\hat{\mu}}{\mu} - 1\right)^2 + \left(\frac{\hat{\sigma}}{\sigma} - 1\right)^2}. \quad (12)$$

366 Here,  $\rho$  is the correlation between model output and observation,  $\hat{\mu}$  and  $\mu$  the modeled  
 367 and observed mean of the streamflow time series, and  $\hat{\sigma}$  and  $\sigma$  the modeled and observed

368 standard deviation of the streamflow time series. This metric is now known as the Kling-  
369 Gupta Efficiency (KGE). The KGE complements RE and CE, and we included the KGE  
370 in model assessment.

371 Conventionally, reconstruction skills are often calculated in a split-sample (i.e., two-  
372 fold) cross-validation scheme: the model is calibrated with the first half of the data and  
373 validated with the second half, then calibrated with the second half and validated with  
374 the first half (see e.g. D'Arrigo et al., 2011). The contiguous halves aim to test a model's  
375 ability to capture a regime shift (Briffa et al., 1988). Unfortunately, this scheme is not  
376 practical for many stations in our record, where it would leave us only 20–25 data points  
377 for calibration (Figure S2). In addition, a two-fold cross-validation scheme provides only  
378 two point estimates for each skill score, and they may be notably different (for exam-  
379 ple, D'Arrigo et al. (2011) reported CE values of 0.21 and 0.73 for the two folds.) As a  
380 result, the mean skill score may not be robust. A number of recent works have instead  
381 used the leave- $k$ -out cross-validation scheme (e.g., Gallant & Gergis, 2011; Ho et al., 2016;  
382 Li et al., 2019). In this scheme, a random chunk of  $k$  data points is withheld for valida-  
383 tion while the model is calibrated with the remaining data points, then calibration and  
384 validation are repeated over as many as 100 chunks of  $k$ . This scheme provides a more  
385 robust estimate of the mean skill score, but it may not correctly assess the model's abil-  
386 ity to capture a regime shift, because the withheld points are not contiguous like in the  
387 split-sample scheme.

388 We sought a balanced approach. In each cross-validation run for each station, we  
389 withheld a *contiguous* chunk of 25% of the data points for validation and trained the model  
390 on the remaining 75%. This way, we maintain the goal of the split-sample scheme while  
391 still having enough data for calibration and getting distributions of skill scores, which  
392 yield a reasonably robust mean skill estimate for each metric. Having distributions of  
393 skill scores has another benefit: we can now make probabilistic statements about skill.  
394 For example, we can calculate the probability that  $CE < 0$ , and if that probability is  
395 less than a threshold  $\alpha$ , say 0.1, then we consider the reconstruction statistically skill-  
396 ful with respect to CE at  $\alpha = 0.1$ . While not doing formal statistical tests, we can make  
397 analogous statements about the significance of the skills scores.

398 When the hold-out chunks are contiguous, there are not as many chunks as when  
399 they are random, so we repeated the procedure 30 times instead of 100, and calculated  
400 the mean RE, CE and KGE over these 30 runs. When calculating the mean scores, we  
401 used the Tukey's biweight robust mean (Mosteller & Tukey, 1977) instead of the arith-  
402 metic mean, to limit the effect of outliers. The robust mean is commonly used by den-  
403 drochronologists to derive the mean chronology from tree ring samples (Cook & Kair-  
404 iukstis, 1990), and we have extended its use here. After cross-validating all ensemble mem-  
405 bers (Section 3.2.1), we selected one member for each station based on the robust mean  
406 CE and KGE (RE is similar to CE and is omitted). The ideal score for both CE and KGE  
407 is 1; therefore, we calculated for each ensemble member the Euclidean distance between  
408 the tuple (CE, KGE) and the point (1, 1). For each station, the ensemble member near-  
409 est to the ideal score was used for the final reconstruction.

## 410 4 Results and Discussion

### 411 4.1 Reconstruction Skills

412 Reduction of Error (RE) is positive at all stations (Figure 4a and b); Coefficient  
 413 of Efficiency (CE) is positive at all but one: Kachora in the Indus (Pakistan), where  $CE \approx$   
 414  $-0.06$  (Figures 4c and d). At  $\alpha = 0.1$ , 30 stations are statistically skillful with respect  
 415 to RE, and 23 are with CE (Figure S9). Comparing the histograms of RE and CE (Fig-  
 416 ures 4b and d), we observe that CE is slightly lower—this is expected as CE is a more  
 417 stringent metric than RE (Cook & Kairiukstis, 1990). Much lower CE than RE implies  
 418 overfitting; we do not observe that here.

419 When using the Kling-Gupta Efficiency (KGE), if one wishes to benchmark a model  
 420 against the verification period mean (as is with the CE), the threshold value is  $1 - \sqrt{2} \approx$   
 421  $-0.41$ , i.e.  $KGE > -0.41$  is analogous to  $CE > 0$  (Knoben et al., 2019). Our KGE  
 422 ranges from 0.22 to 0.68 (Figure 4e and f), far higher than the threshold. Furthermore,  
 423 all 62 stations are statistically skillful with respect to KGE at  $\alpha = 0.1$  (Figure S9). These  
 424 results indicate that our reconstruction model performs well in terms of key character-  
 425 istics: correlation, bias, and variability.

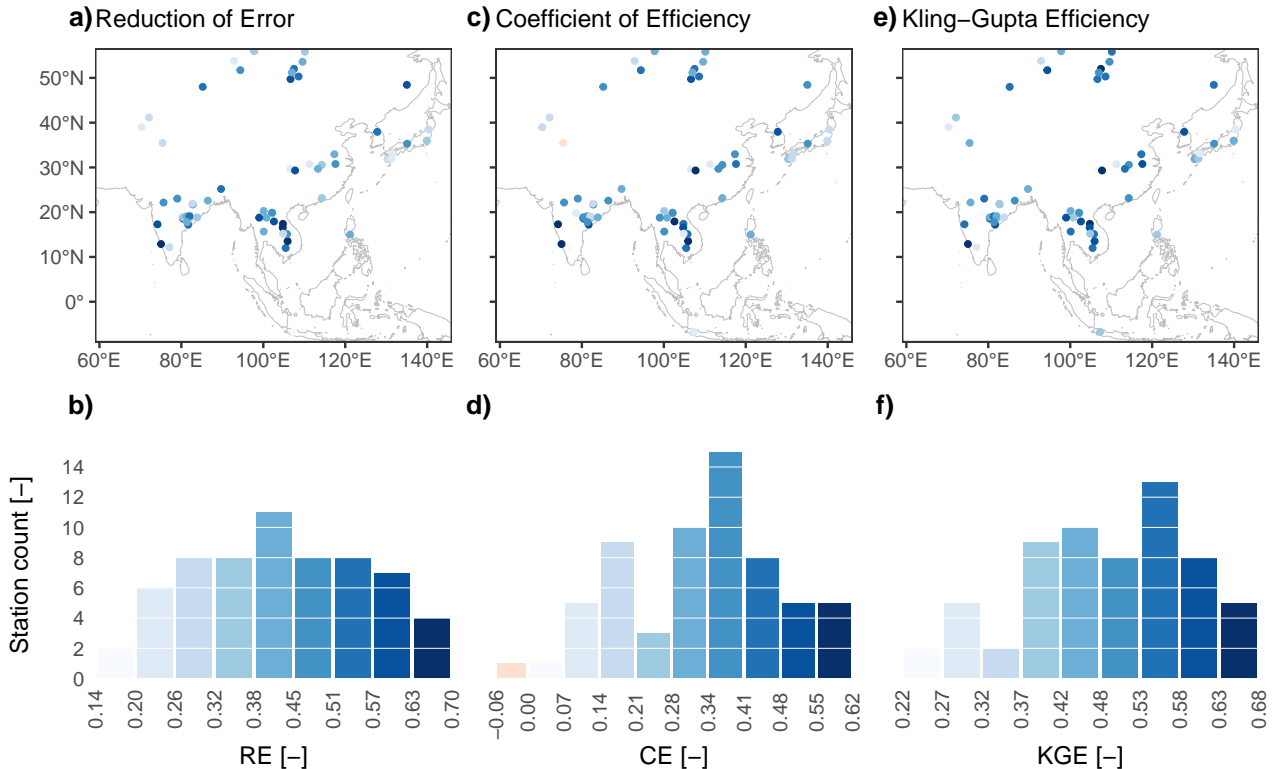


**Figure 4.** Distribution of model performance scores. Panels a, c, and e show the scores of each station following the color legends encoded with the histograms in panels b, d, and f.

426 All three metrics have similar spatial distributions (Figure 4a, c, and e). As expected,  
 427 lower skills are seen in most of Central Asia, Japan, and West Asia, which lie outside the  
 428 core monsoon area. An exception is the upper reach of the Selenge River, upstream of  
 429 Lake Baikal, where model skill is high, owing to high quality tree ring records from Mon-  
 430 golia (Davi et al., 2006; Pederson et al., 2013; Davi et al., 2013; Pederson et al., 2014).  
 431 In all other regions, model skill is homogeneous. The consistent performance of our model  
 432 suggests that the MADA is a good proxy for streamflow reconstruction in Asia, and our  
 433 climate-informed dynamic reconstruction is skillful. More validation exercises (Figures  
 434 S5 to S8) further support the reliability of the reconstruction.

## 435 4.2 Spatiotemporal Variability of Monsoon Asia’s Streamflow

436 Having obtained reliable skill scores, we now present eight centuries of spatiotem-  
 437 poral streamflow variability in Monsoon Asia, in terms of standardized streamflow ( $z$ -  
 438 score of mean annual flow) (Figure 5a). This reconstructed history captures the ripar-  
 439 ian footprint of major historical events—large volcanic eruptions and megadroughts (Fig-  
 440 ure 5b). We first discuss the impact of the three largest eruptions of the past eight cen-  
 441 turies (Sigl et al., 2015): Samalas (1257) (Lavigne et al., 2013), Kuwae (1452-53) (Gao  
 442 et al., 2006), and Tambora (1815) (Stothers, 1984).

443 Assuming that Kuwae erupted in 1452 (consistent with tree ring records, see e.g.  
 444 Briffa et al. (1998)), these three eruptions saw similar streamflow patterns (Figure 5b,  
 445 panels 1, 4, and 8). In the eruption year  $t$  ( $t = 1257, 1452, 1815$ ), large positive stream-  
 446 flow anomalies were observed in Southeast and East Asia. The magnitude of the posi-  
 447 tive anomalies were largest with Samalas, followed by Kuwae, and then Tambora. The  
 448 global radiative forcings of the Samalas, Kuwae, and Tambora events are  $-32.8$ ,  $-20.5$ ,  
 449 and  $-17.1$   $\text{W}/\text{m}^2$ , respectively (Sigl et al., 2015). Thus, we observe a correspondence be-  
 450 tween the magnitude of positive streamflow anomalies and the magnitude of radiative  
 451 forcings. This correspondence are also seen clearly from the distributions of streamflow  
 452 anomalies in the three events (Figure S10a). These results suggest a direct influence of  
 453 volcanic eruptions on streamflow in Southeast and East Asia.

454 Unlike East and Southeast Asia, South Asia’s streamflow remained around the nor-  
 455 mal level in years  $t$  and  $t+1$  in all three eruptions, suggesting little volcanic influence.  
 456 Differently still, mixed wet and dry conditions were observed in Central Asia, and nor-  
 457 mal to wet conditions were observed in eastern China and West Asia (see also Figure S10a).  
 458 Thus, the influence of volcanic eruptions on Monsoon Asia’s streamflow varies spatially,  
 459 ranging from strong positive, mixed, to little. Understanding the mechanism underly-  
 460 ing this spatial variability could be an interesting research direction.

461 Our results are mostly consistent with Anchukaitis et al. (2010), who used Super-  
 462 posed Epoch Analysis to analyze PDSI anomalies in the eruption years. The key differ-  
 463 ence is in eastern China, where Anchukaitis et al. (2010) showed negative PDSI in year  
 464  $t$ , while we observed normal to positive streamflow anomalies in year  $t$ , and negative stream-  
 465 flow anomalies in year  $t + 1$  (see also Figure S10b). The discrepancies may be due to  
 466 the different eruption data sets (Anchukaitis et al. (2010) demonstrated this with three

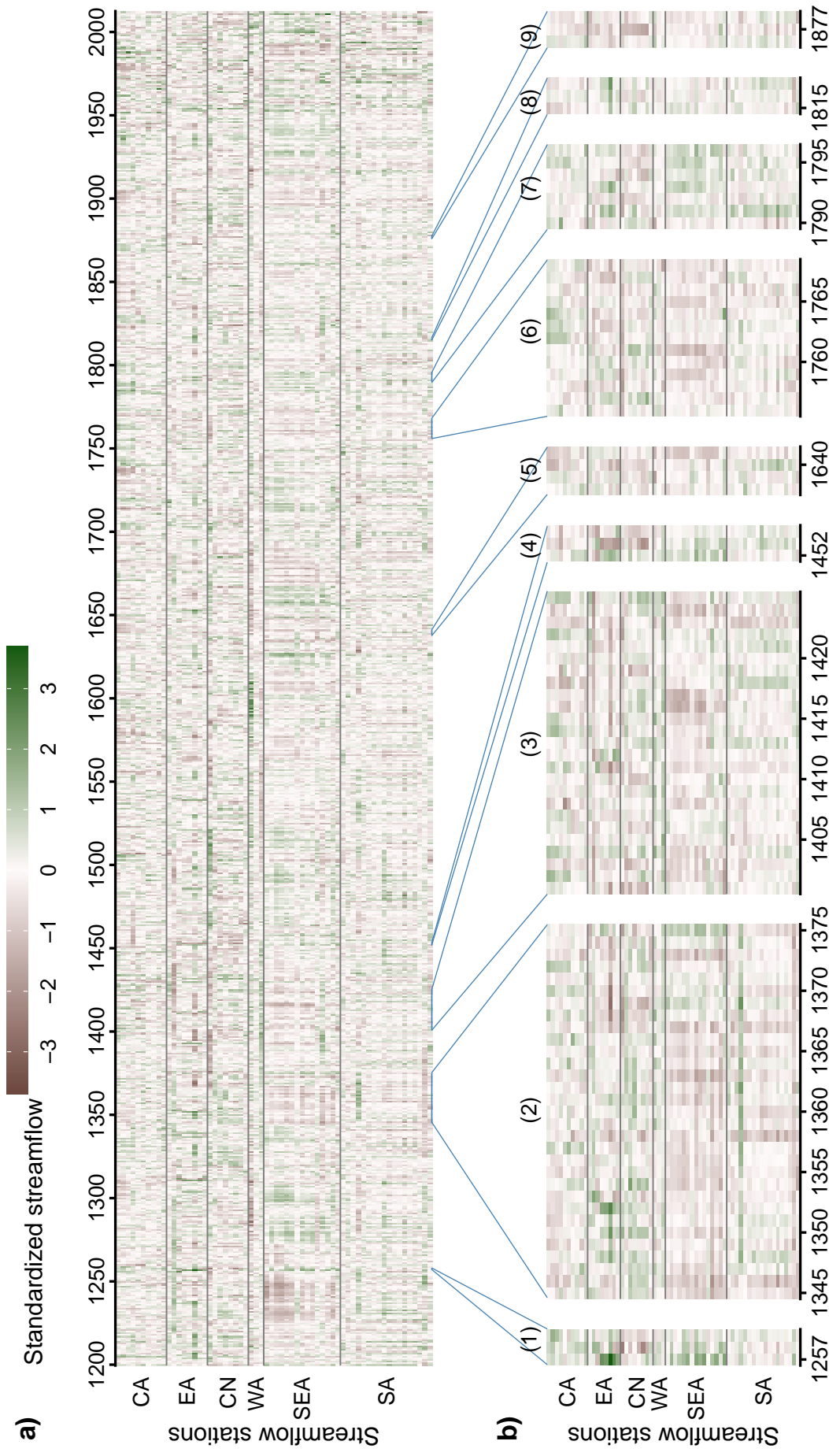


**Figure 5.** Spatiotemporal variability of streamflow in Monsoon Asia. a) Variations over time (x-axis) and space (y-axis) of the standardized streamflow index (i.e., z-score of streamflow, or z-score of log-transformed streamflow when log-transformation was used in the reconstruction). The stations are arranged approximately north to south (top down on y-axis) and divided into five regions as delineated in Figure 1: CA (Central Asia), EA (East Asia), WA (West Asia), CN (eastern China), SEA (Southeast Asia), and SA (South Asia). b) Historic events captured in the reconstruction: (1) Samalas eruption, (2) and (3) Angkor Droughts I and II, (4) Kiuwae eruption, (5) Ming Dynasty Drought, (6) East India Drought, (7) Strange Parallels Drought, (8) Tambora eruption, and (9) Victorian Great Drought.

sets of events) and the analytical methods. It could also be because they analyzed PDSI while we analyzed streamflow. That we observed negative streamflow anomalies in year  $t + 1$  instead of  $t$  could be due to the lagged response of streamflow in this region.

As a drought/pluvial indicator, streamflow may differ from PDSI in individual years for some regions, as discussed above, but on longer terms, our reconstructed streamflow agrees well with reconstructed PDSI. For example, our record fully captures the Angkor Droughts (1345–1374 and 1401–1425) (Buckley et al., 2010, 2014) with prolonged low flow throughout Southeast Asia, and extended as far as India (Figure 5b, panels 2 and 3), in agreement with speleothem records from Dandak and Jhuma Caves (Sinha et al., 2007, 2011). Heavy monsoon rain interrupted these megadroughts; such abrupt alterations to the flow regime proved difficult for the ancient city of Angkor (Buckley et al., 2014). The city once thrived thanks to an extensive network of hydraulic infrastructure (Lieberman & Buckley, 2012). After the first Angkor Drought, the inflow/outflow functions of the *barays* (reservoirs) were altered in an attempt to preserve water. Heavy rains and flooding subsequently destroyed the reduced-capacity hydraulic infrastructure. This flood likely occurred in 1375 (Figure 5b, event 2). By the second Angkor Drought, the “hydraulic city” (Groslier, 1979; Lustig & Pottier, 2007) had insufficient water storage and could not recover.

Four more megadroughts that severely affected Asian societies (Cook et al., 2010) are also captured in our reconstruction (Figure 5b, panels 5, 6, 7, and 9), along with other major droughts and pluvials. For example, Central Asia observed a six-decade drought between 1260–1320, and sustained pluvials during 1740–1769. Most notably, Southeast Asia suffered a drought between 1225–1255 that was comparable in length to Angkor Drought I, but more severe in magnitude. Following this drought was a multi-decadal pluvial in 1271–1307. The drought is prominent in the speleothem record of J. K. Wang et al. (2019), and the pluvial can also be traced from there.

### 4.3 Links to Oceanic Drivers

To exemplify the spatial variation of how the oceans influence streamflow, we selected four river basins from west to east: Godavari, Chao Phraya, Mekong, and Yangtze, and selected one station from each basin. The selected stations are in the main stream and their reconstructions are statistically skillful.

We calculated the correlation between reconstructed annual streamflow at each station and the seasonal averages of global sea surface temperature (SST) for the period 1856–2012. The season definitions are: December to February (DJF), March to May (MAM), June to August (JJA), and September to November (SON). We also included JJA and SON of the prior year (JJA ( $-1$ ) and SON ( $-1$ )). Correlation patterns vary both seasonally and spatially, with differences among rivers and among oceans (Figure 6).

### 504 **4.3.1 Pacific Ocean**

505 Tropical Pacific SST correlates significantly with streamflow at all four basins, but  
 506 the correlation patterns vary. For the Godavari, moderate positive correlations are seen  
 507 from JJA (−1) to DJF, and strong negative correlations are seen from JJA to SON. For  
 508 the Yangtze, the pattern is completely opposite: strong positive correlations from JJA  
 509 (−1) to DJF, and moderate negative correlations in JJA and SON. The location of the  
 510 strongest correlations suggests links to the El Niño-Southern Oscillation (ENSO, cf. McPhaden  
 511 et al. (2006)). We find it interesting that ENSO seems to influence the Godavari and Yangtze  
 512 in contrasting ways.

513 Unlike the Godavari and Yangtze, the Chao Phraya and Mekong’s streamflow cor-  
 514 relates significantly with SST over most of the Pacific Ocean, and the correlation per-  
 515 sists across all seasons. The correlation pattern is negative in the tropical Pacific, and  
 516 positive in the northern and southern Pacific. This pattern and its lack of seasonality  
 517 suggest that, beside ENSO, there are influences from a driver at longer time scales, likely  
 518 the Pacific Decadal Variability (PDV)—decadal variations of Pacific SST resulted from  
 519 complex tropical-extratropical ocean-atmosphere interactions (Henley, 2017). The North  
 520 Pacific component of PDV is known as the Pacific Decadal Oscillation (PDO) (Mantua  
 521 & Hare, 2002), its southern counterpart the South Pacific Decadal Oscillation (Shakun  
 522 & Shaman, 2009); basin-wide SST variation patterns have also been termed Interdecadal  
 523 Pacific Oscillation (Folland et al., 1999). These modes are closely related (Henley, 2017).  
 524 The PDV has been shown to influence hydroclimatic variability in Monsoon Asia, in con-  
 525 junction with ENSO (Yu et al., 2018). Specifically for the Chao Phraya, PDV also mod-  
 526 ulates ENSO’s influence on peak flow (Xu et al., 2019).

### 527 **4.3.2 Indian Ocean**

528 Correlation patterns are less prominent in the Indian Ocean compared to the Pa-  
 529 cific. We observe basin-wide correlations in DJF for the Godavari and Yangtze; corre-  
 530 lations bear the same sign as that in the Pacific. This is consistent with the Indo-Pacific  
 531 coupling: an ENSO event in the Pacific leads to SST anomalies of the same sign in the  
 532 Indian Ocean (Saji et al., 1999). The Godavari and Yangtze also exhibit another cor-  
 533 relation pattern in SON (with small areas of significance): correlations bear opposite signs  
 534 between the tropical western Indian Ocean near the Horn of Africa and the southeast-  
 535 ern Indian Ocean around Sumatra. This pattern and its timing suggest links to the In-  
 536 dian Ocean Dipole (IOD) (Saji et al., 1999; Ummenhofer et al., 2017). The IOD accounts  
 537 for about 12% of Indian Ocean SST variability, much less than the basin-wide coupling  
 538 mode (30%) (Saji et al., 1999); this explains the weaker correlations of the IOD. Pos-  
 539 itive IOD events have also been linked to droughts in Southeast Asia, but this relation-  
 540 ship is not robust (Ummenhofer et al., 2013). In our analysis, the link between IOD and  
 541 Southeast Asian streamflow is not visible. Our interpretation is that ENSO and PDV  
 542 are the main drivers here, and they dominate any links that the IOD might have.

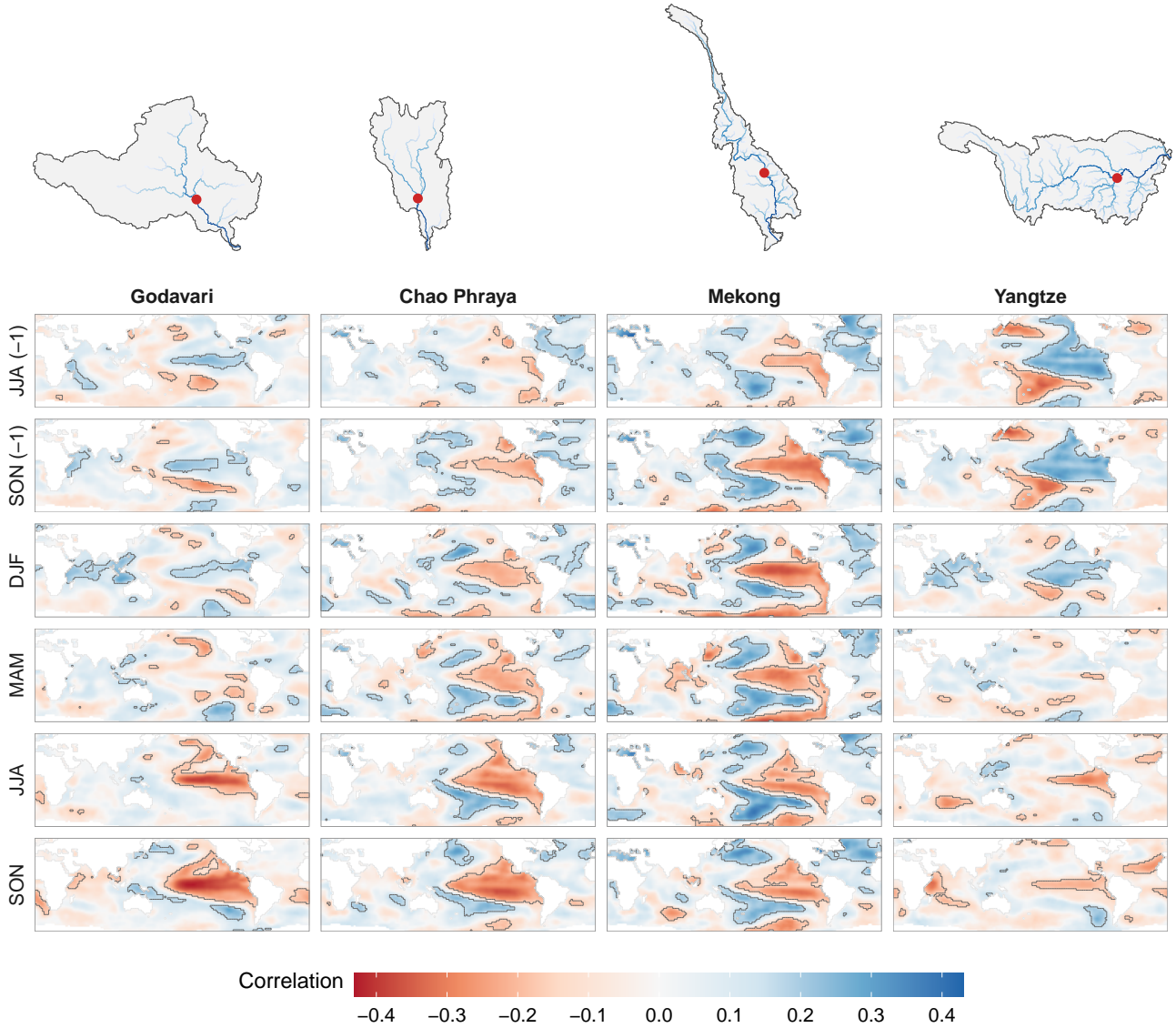


**Figure 6.** Correlation between reconstructed mean annual streamflow at four river basins (this work) and seasonal averages of global sea surface temperature (SST) from the NOAA\_ERSST\_v5 data set (Huang et al., 2017) for the period 1856–2012; significant correlations ( $\alpha = 0.05$ ) enclosed in black boundaries. The locations of the stations are shown in the catchment maps; these are the same stations shown in Figure 3. Seasons are marked by the year in which they end. “(-1)” denotes previous year.

543

### 4.3.3 Atlantic Ocean

544

545

546

547

The Chao Phraya and Mekong streamflow correlates positively with tropical and northern Atlantic SST. Significant and consistent correlations are observed throughout the seasons for the Mekong, but less consistent for the Chao Phraya. The link between tropical Atlantic SST and Southeast Asian hydroclimate was also found in a Laotian cave

548 speleothem record (J. K. Wang et al., 2019). To explain this relationship, J. K. Wang  
549 et al. (2019) examined SST, atmospheric pressure, and zonal moisture transport from  
550 climate model simulations, and proposed the following mechanism: increased tropical  
551 Atlantic SST leads to changes in zonal moisture transport, causing depression over trop-  
552 ical Indian Ocean, reducing rainout over the basin, leaving more moisture available to  
553 be transported to mainland Southeast Asia, ultimately strengthening Indian Monsoon  
554 rain over the region.

555 We repeated the correlation analysis above for other stations in the Godavari, Mekong,  
556 and Yangtze, where additional stations with statistically skillful results are available on  
557 the main stream. Results for those stations are consistent with what we report here (Fig-  
558 ures S11 to S13).

#### 559 *4.3.4 Temporal variability of teleconnections*

560 The correlation analysis of Figure 6 shows the spatial variation of the streamflow–  
561 SST teleconnection in Monsoon Asia. This analysis was done for the common period of  
562 SST and streamflow data (1856–2012). To explore whether and how the teleconnection  
563 patterns changed through time, we repeated the correlation analysis using a sliding 50-  
564 year window with 10-year increments. We show in Figure 7 three non-overlapping win-  
565 dows, and present all windows in Movie S1. Results show that all correlation patterns  
566 changed through time, echoing previous works that found non-stationarities in oceanic  
567 teleconnection (e.g., Krishna Kumar et al. (1999); Singhrattna et al. (2005)). Correla-  
568 tions were much weaker in the period 1911–1960 compared to the preceding and sub-  
569 sequent five decades (Figure 7). Some patterns are more transient than others. The Yangtze’s  
570 JJA–SON pattern of negative correlations with tropical Pacific was only strong in 1921–  
571 1980 (Movie S1). On the other hand, the Chao Phraya’s SON positive correlations with  
572 tropical Pacific persisted throughout all periods. In 1901–1950, when ENSO teleconnec-  
573 tion was the weakest for all rivers, tropical and northern Atlantic SST became the strongest  
574 teleconnection for the Chao Phraya and Mekong (Movie S1).

## 575 **5 Conclusions**

576 In this work, we produce the first large-scale and long-term record of streamflow  
577 variability for Monsoon Asia, covering 62 stations in 16 countries. In making this record,  
578 we also develop a novel automated, climate-informed, and dynamic streamflow recon-  
579 struction framework that leverages the computational advantages offered by our climate  
580 proxy—the Monsoon Asia Drought Atlas (MADA) version 2. Our framework achieves  
581 good skills for most of Monsoon Asia, and skill distribution is spatially homogeneous.  
582 Our results provide a synoptic understanding of Monsoon Asia’s streamflow variability  
583 over the past eight centuries, and reveal how the teleconnection between streamflow and  
584 its oceanic drivers varied over space and time.

585 From our reconstruction, streamflow in Monsoon Asia appears coherent: high and  
586 low flows often occur simultaneously at nearby stations and adjacent basins. This co-

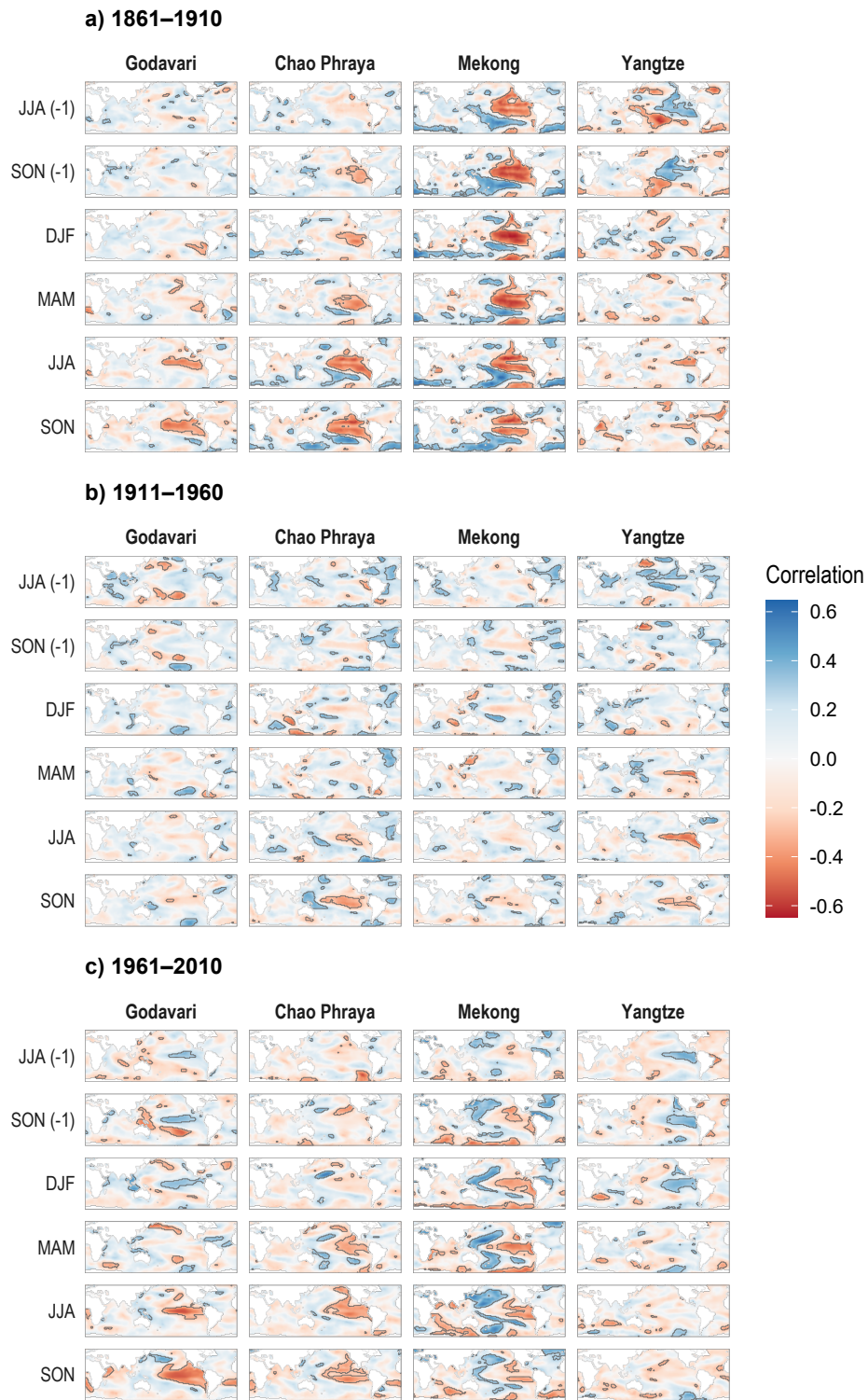


**Figure 7.** Temporal variability of the streamflow–sea surface temperature correlations. The analysis here is the same as that carried out in Figure 6, but split into three 50-year periods.

587 herence is attributed to common oceanic drivers—the El Niño–Southern Oscillation (ENSO),  
588 the Pacific Decadal Variability (PDV), and sea surface temperature variations in the In-  
589 dian and Atlantic Oceans. Coherence emerges even though we reconstructed each sta-  
590 tion individually, demonstrating the merits of Point-by-Point Regression. More impor-  
591 tantly, this coherence implies that large-scale infrastructure transferring water, or other  
592 water-reliant commodities, across river basins could accidentally expose riparian people  
593 to unforeseen risks. For example, Thailand is increasingly purchasing Mekong-generated  
594 hydropower from Laos, and when that is insufficient, complements its energy needs with  
595 thermal power from plants that use water from the Chao Phraya for cooling. Thailand’s  
596 energy system is more vulnerable when a prolonged drought occurs at both rivers (Chowdhury  
597 et al., 2020)—our record shows such events have happened several times in the past.

598 We showed that the Pacific, Indian, and Atlantic Oceans influence streamflow vari-  
599 ability, and that the strength and spatial footprint of these teleconnections varied over  
600 time. This result suggests that our understanding of how water-dependent infrastruc-  
601 ture could perform may be narrow, especially in South and Southeast Asia, where we  
602 observe alternating periods of strong and weak teleconnections. A narrow characteriza-  
603 tion of climate-induced risks is likely to misguide climate change assessments, an impor-  
604 tant source of information for many major infrastructural decisions. Stakes are partic-  
605 ularly high in Monsoon Asia, whose river basins will experience further pressure in the  
606 coming decades (Sato et al., 2017; Y. Wang et al., 2019). If we can develop method-  
607 ologies for viewing future changes in streamflow in the context of past and present cli-  
608 mate, we then have a pathway for making more informed and robust decisions. The re-  
609 constructions developed in our study offer a first step in this direction.

## 610 **Acknowledgments**

611 Hung Nguyen is supported by the President’s Graduate Fellowship from the Singapore  
612 University of Technology and Design. We thank Edward Cook, Caroline Ummenhofer,  
613 Nerilie Abram, Nathalie Goodkin, Xun Sun, Murray Peel, Rory Nathan, and Robert Was-  
614 son for insightful comments. We are indebted to Michelle Ho, Justin Maxwell, Valerie  
615 Trouet, two anonymous reviewers, and the Associate Editor for their constructive reviews.  
616 We are grateful to Thanh Dang, Mukund Rao, Christoph Libisch-Lehner, Rosanne D’Arrigo,  
617 Donghoon Lee, and Caroline Leland for streamflow data of the Mekong, Brahmaputra,  
618 Angat, Citarum, Han, and Yeruu Rivers. Chao Phraya River data were obtained from  
619 the Thai Royal Irrigation Department at [www.hydro1.net](http://www.hydro1.net), Indus River from Rao et al.  
620 (2018, Supporting Information), other streamflow data from GSIM (Do et al., 2018; Gud-  
621 mundsson et al., 2018), reservoir data from GRanD v1.3 (Lehner et al., 2011), MADA  
622 v2 data from Marvel et al. (2019) at [www.dropbox.com/s/n21o99h9qn17prg/madaV2.nc](http://www.dropbox.com/s/n21o99h9qn17prg/madaV2.nc),  
623 river network data from FLO1K (Barbarossa et al., 2018) with help postprocessing by  
624 Valerio Barbarossa, basin boundary data from HydroSHEDS (Lehner & Grill, 2013) at  
625 [hydrosheds.org](http://hydrosheds.org), SST data from NOAA ERSST v5 (Huang et al., 2017) provided by  
626 the NOAA/OAR/ESRL PSD, Boulder, Colorado, USA, at [www.esrl.noaa.gov/psd/](http://www.esrl.noaa.gov/psd/).  
627 This work was conducted with open-source software: analysis and visualization performed  
628 in R (R Core Team, 2019), maps made in QGIS, and manuscript written in LaTeX. We  
629 thank the open-source software community, especially the R package creators and main-

630 tainers, for their contributions to open science. We provide all data, documented code,  
 631 and results at <https://github.com/ntthung/paleo-asia> (DOI: 10.5281/zenodo.3818117);  
 632 exceptions are instrumental data of the Mekong, Yangtze, and Pearl Rivers due to re-  
 633 strictions. Lamont contribution number XXXX.

## 634 References

- 635 Adams, K. D., Negrini, R. M., Cook, E. R., & Rajagopal, S. (2015, dec). Annually  
 636 resolved late Holocene paleohydrology of the southern Sierra Nevada and Tu-  
 637 lare Lake, California. *Water Resources Research*, *51*(12), 9708–9724. DOI:  
 638 10.1002/2015WR017850
- 639 Allen, K. J., Nichols, S. C., Evans, R., Allie, S., Carson, G., Ling, F., . . . Baker,  
 640 P. J. (2017, jan). A 277 year cool season dam inflow reconstruction for Tasma-  
 641 nia, southeastern Australia. *Water Resources Research*, *53*(1), 400–414. DOI:  
 642 10.1002/2016WR018906
- 643 Anchukaitis, K. J., Buckley, B. M., Cook, E. R., Cook, B. I., D’Arrigo, R. D., &  
 644 Ammann, C. M. (2010). Influence of volcanic eruptions on the climate of  
 645 the Asian monsoon region. *Geophysical Research Letters*, *37*(22), 1–5. DOI:  
 646 10.1029/2010GL044843
- 647 Barbarossa, V., Huijbregts, M. A., Beusen, A. H., Beck, H. E., King, H., & Schipper,  
 648 A. M. (2018, mar). FLO1K, global maps of mean, maximum and minimum  
 649 annual streamflow at 1 km resolution from 1960 through 2015. *Scientific Data*,  
 650 *5*(October 2017), 180052. DOI: 10.1038/sdata.2018.52
- 651 Best, J. (2019). Anthropogenic stresses on the world’s big rivers. *Nature Geoscience*,  
 652 *12*(1), 7–21. DOI: 10.1038/s41561-018-0262-x
- 653 Boers, N., Goswami, B., Rheinwalt, A., Bookhagen, B., Hoskins, B., & Kurths,  
 654 J. (2019, jan). Complex networks reveal global pattern of extreme-rainfall  
 655 teleconnections. *Nature*. DOI: 10.1038/s41586-018-0872-x
- 656 Briffa, K. R., Jones, P. D., Pilcher, J. R., & Hughes, M. K. (1988, nov). Recon-  
 657 structing Summer Temperatures in Northern Fennoscandia Back to A.D.  
 658 1700 Using Tree-Ring Data from Scots Pine. *Arctic and Alpine Research*,  
 659 *20*(4), 385. DOI: 10.2307/1551336
- 660 Briffa, K. R., Jones, P. D., Schweingruber, F. H., & Osborn, T. J. (1998). Influence  
 661 of volcanic eruptions on Northern Hemisphere summer temperature over the  
 662 past 600 years. *Nature*, *393*(6684), 450–455. DOI: 10.1038/30943
- 663 Buckley, B. M., Anchukaitis, K. J., Penny, D., Fletcher, R., Cook, E. R., Sano, M.,  
 664 . . . Hong, T. M. (2010, apr). Climate as a contributing factor in the demise of  
 665 Angkor, Cambodia. *Proceedings of the National Academy of Sciences*, *107*(15),  
 666 6748–6752. DOI: 10.1073/pnas.0910827107
- 667 Buckley, B. M., Fletcher, R., Wang, S. Y. S., Zottoli, B., & Pottier, C. (2014).  
 668 Monsoon extremes and society over the past millennium on main-  
 669 land Southeast Asia. *Quaternary Science Reviews*, *95*, 1–19. DOI:  
 670 10.1016/j.quascirev.2014.04.022
- 671 Chen, F., He, Q., Bakytbek, E., Yu, S., & Zhang, R. (2017, nov). Reconstruc-

- 672 tion of a long streamflow record using tree rings in the upper Kurshab River  
673 (Pamir-Alai Mountains) and its application to water resources management.  
674 *International Journal of Water Resources Development*, 33(6), 976–986. DOI:  
675 10.1080/07900627.2016.1238347
- 676 Chen, F., Shang, H., Panyushkina, I., Meko, D., Li, J., Yuan, Y., . . . Luo, X. (2019,  
677 aug). 500-year tree-ring reconstruction of Salween River streamflow related to  
678 the history of water supply in Southeast Asia. *Climate Dynamics*(0123456789).  
679 DOI: 10.1007/s00382-019-04948-1
- 680 Chen, F., Shang, H., Panyushkina, I. P., Meko, D. M., Yu, S., Yuan, Y., & Chen, F.  
681 (2019, may). Tree-ring reconstruction of Lhasa River streamflow reveals 472  
682 years of hydrologic change on southern Tibetan Plateau. *Journal of Hydrology*,  
683 572, 169–178. DOI: 10.1016/j.jhydrol.2019.02.054
- 684 Chen, F., Yuan, Y., Davi, N. K., & Zhang, T. (2016, dec). Upper Irtysh River  
685 flow since AD 1500 as reconstructed by tree rings, reveals the hydrocli-  
686 matic signal of inner Asia. *Climatic Change*, 139(3-4), 651–665. DOI:  
687 10.1007/s10584-016-1814-y
- 688 Chen, F., & Yuan, Y.-j. (2016, jul). Streamflow reconstruction for the Guxi-  
689 ang River, eastern Tien Shan (China): linkages to the surrounding rivers  
690 of Central Asia. *Environmental Earth Sciences*, 75(13), 1049. DOI:  
691 10.1007/s12665-016-5849-1
- 692 Chen, F., Yuan, Y.-j., Zhang, R.-b., Wang, H.-q., Shang, H.-m., Zhang, T.-w., . . .  
693 Fan, Z.-a. (2016, jun). Shiyang River streamflow since AD 1765, reconstructed  
694 by tree rings, contains far-reaching hydro-climatic signals over and beyond  
695 the mid-latitude Asian continent. *Hydrological Processes*, 30(13), 2211–2222.  
696 DOI: 10.1002/hyp.10788
- 697 Chowdhury, A. F. M., Dang, T. D., Bagchi, A., & Galelli, S. (2020). Expected  
698 benefits of Laos’ hydropower development curbed by hydro-climatic variability  
699 and limited transmission capacity—opportunities to reform. *Journal of Water*  
700 *Resources Planning and Management*.
- 701 Cook, E. R. (2015). *Developing MADAv2 Using The Point-*  
702 *By-Point Regression Climate Field Reconstruction Method*.  
703 Kyoto, Japan: 4th Asia 2k Workshop. Retrieved from  
704 [http://pastglobalchanges.org/download/docs/working{\\\_}groups/asia2k/4thAsia2k/Cook.ppsx](http://pastglobalchanges.org/download/docs/working{\_}groups/asia2k/4thAsia2k/Cook.ppsx)  
705
- 706 Cook, E. R., Anchukaitis, K. J., Buckley, B. M., D’Arrigo, R. D., Jacoby, G. C.,  
707 & Wright, W. E. (2010, apr). Asian Monsoon Failure and Megadrought  
708 During the Last Millennium. *Science*, 328(5977), 486–489. DOI:  
709 10.1126/science.1185188
- 710 Cook, E. R., & Kairiukstis, L. A. (1990). *Methods of dendrochronology. Applications*  
711 *in the Environmental Sciences* (E. R. Cook & L. A. Kairiukstis, Eds.). Kluwer  
712 Academic Publishers.
- 713 Cook, E. R., Meko, D. M., Stahle, D. W., & Cleaveland, M. K.  
714 (1999). Drought Reconstructuions for the continental United  
715 States. *Journal of Climate*, 12(APRIL), 1145–1162. DOI:

- 10.1175/1520-0442(1999)012<1145:DRFTCU>2.0.CO;2
- 716 Cook, E. R., Palmer, J. G., Ahmed, M., Woodhouse, C. A., Fenwick, P., Zafar,  
717 M. U., . . . Khan, N. (2013). Five centuries of Upper Indus River flow  
718 from tree rings. *Journal of Hydrology*, *486*(August 2018), 365–375. DOI:  
719 10.1016/j.jhydrol.2013.02.004
- 720 Cook, E. R., Seager, R., Kushnir, Y., Briffa, K. R., Büntgen, U., Frank, D., . . .  
721 Zang, C. (2015). Old World megadroughts and pluvials during the Common  
722 Era. *Science Advances*, *1*(10), 1–10. DOI: 10.1126/sciadv.1500561
- 723 Cook, E. R., Solomina, O., Matkovsky, V., Cook, B. I., Agafonov, L., Berd-  
724 nikova, A., . . . Yermokhin, M. (2020, feb). The European Russia Drought  
725 Atlas (14002016 CE). *Climate Dynamics*, *54*(3-4), 2317–2335. DOI:  
726 10.1007/s00382-019-05115-2
- 727 Coulthard, B., Smith, D. J., & Meko, D. M. (2016, mar). Is worst-case scenario  
728 streamflow drought underestimated in British Columbia? A multi-century per-  
729 spective for the south coast, derived from tree-rings. *Journal of Hydrology*,  
730 *534*, 205–218. DOI: 10.1016/j.jhydrol.2015.12.030
- 731 Dai, A., Trenberth, K. E., & Qian, T. (2004). A Global Dataset of Palmer Drought  
732 Severity Index for 18702002: Relationship with Soil Moisture and Effects of  
733 Surface Warming. *Journal of Hydrometeorology*, *5*(6), 1117–1130. DOI:  
734 10.1175/JHM-386.1
- 735 D’Arrigo, R., Abram, N. J., Ummenhofer, C., Palmer, J., & Mudelsee, M. (2011,  
736 feb). Reconstructed streamflow for Citarum River, Java, Indonesia: linkages  
737 to tropical climate dynamics. *Climate Dynamics*, *36*(3-4), 451–462. DOI:  
738 10.1007/s00382-009-0717-2
- 739 Davi, N. K., Jacoby, G. C., Curtis, A. E., & Baatarbileg, N. (2006). Extension of  
740 drought records for central Asia using tree rings: West-central Mongolia. *Jour-  
741 nal of Climate*, *19*(1), 288–299. DOI: 10.1175/JCLI3621.1
- 742 Davi, N. K., Pederson, N., Leland, C., Nachin, B., Suran, B., & Jacoby, G. C.  
743 (2013). Is eastern Mongolia drying? A long-term perspective of a mul-  
744 tidecadal trend. *Water Resources Research*, *49*(1), 151–158. DOI:  
745 10.1029/2012WR011834
- 746 DeRose, R., Bekker, M. F., Wang, S.-Y., Buckley, B. M., Kjølgren, R., Bardsley,  
747 T., . . . Allen, E. (2015, oct). A millennium-length reconstruction of Bear  
748 River stream flow, Utah. *Journal of Hydrology*, *529*(P2), 524–534. DOI:  
749 10.1016/j.jhydrol.2015.01.014
- 750 Do, H. X., Gudmundsson, L., Leonard, M., & Westra, S. (2018, apr). The Global  
751 Streamflow Indices and Metadata Archive (GSIM) Part 1: The production of  
752 a daily streamflow archive and metadata. *Earth System Science Data*, *10*(2),  
753 765–785. DOI: 10.5194/essd-10-765-2018
- 754 Folland, C. K., Parker, D. E., Colman, A. W., & Washington, R. (1999). Large Scale  
755 Modes of Ocean Surface Temperature Since the Late Nineteenth Century. In  
756 *Beyond el niño* (pp. 73–102). Berlin, Heidelberg: Springer Berlin Heidelberg.  
757 DOI: 10.1007/978-3-642-58369-8\_4
- 758 Fritts, H. C. (1976). *Tree Rings and Climate*. London: Elsevier. DOI:  
759

- 760 10.1016/B978-0-12-268450-0.X5001-0
- 761 Gallant, A. J. E., & Gergis, J. (2011). An experimental streamflow reconstruction  
762 for the River Murray, Australia, 1783-1988. *Water Resources Research*, *47*(4),  
763 1–15. DOI: 10.1029/2010WR009832
- 764 Gao, C., Robock, A., Self, S., Witter, J. B., Steffenson, J. P., Clausen, H. B., ...  
765 Ammann, C. (2006). The 1452 or 1453 A.D. Kuwae eruption signal derived  
766 from multiple ice core records: Greatest volcanic sulfate event of the past 700  
767 years. *Journal of Geophysical Research Atmospheres*, *111*(12), 1–11. DOI:  
768 10.1029/2005JD006710
- 769 Genuer, R., Poggi, J.-m., & Tuleau-Malot, C. (2010, oct). Variable selection using  
770 random forests. *Pattern Recognition Letters*, *31*(14), 2225–2236. DOI:  
771 10.1016/j.patrec.2010.03.014
- 772 Gou, X., Chen, F., Cook, E. R., Jacoby, G., Yang, M., & Li, J. (2007). Stream-  
773 flow variations of the Yellow River over the past 593 years in western China  
774 reconstructed from tree rings. *Water Resources Research*, *43*(6), 1–9. DOI:  
775 10.1029/2006WR005705
- 776 Gou, X. H., Deng, Y., Chen, F. H., Yang, M. X., Fang, K. Y., Gao, L. L., ... Zhang,  
777 F. (2010). Tree ring based streamflow reconstruction for the Upper Yellow  
778 River over the past 1234 years. *Chinese Science Bulletin*, *55*(36), 4179–4186.  
779 DOI: 10.1007/s11434-010-4215-z
- 780 Graham, N. E., & Hughes, M. K. (2007, dec). Reconstructing the Mediaeval low  
781 stands of Mono Lake, Sierra Nevada, California, USA. *The Holocene*, *17*(8),  
782 1197–1210. DOI: 10.1177/0959683607085126
- 783 Groslier, B. P. (1979). La cité hydraulique angkoriennne: exploitation ou surexploita-  
784 tion du sol ? *Bulletin de l'Ecole française d'Extrême-Orient*, *66*(1), 161–202.  
785 DOI: 10.3406/befeo.1979.4014
- 786 Gudmundsson, L., Do, H. X., Leonard, M., & Westra, S. (2018, apr). The Global  
787 Streamflow Indices and Metadata Archive (GSIM) Part 2: Quality control,  
788 time-series indices and homogeneity assessment. *Earth System Science Data*,  
789 *10*(2), 787–804. DOI: 10.5194/essd-10-787-2018
- 790 Güner, H. T., Köse, N., & Harley, G. L. (2017). A 200-year reconstruction of Ko-  
791 casu River (Sakarya River Basin, Turkey) streamflow derived from a tree-ring  
792 network. *International Journal of Biometeorology*, *61*(3), 427–437. DOI:  
793 10.1007/s00484-016-1223-y
- 794 Gupta, H. V., Kling, H., Yilmaz, K. K., & Martinez, G. F. (2009, oct). Decompo-  
795 sition of the mean squared error and NSE performance criteria: Implications  
796 for improving hydrological modelling. *Journal of Hydrology*, *377*(1-2), 80–91.  
797 DOI: 10.1016/j.jhydrol.2009.08.003
- 798 Hart, S. J., Smith, D. J., & Clague, J. J. (2010, sep). A multi-species dendroclimatic  
799 reconstruction of Chilko River streamflow, British Columbia, Canada. *Hydro-  
800 logical Processes*, *24*(19), 2752–2761. DOI: 10.1002/hyp.7674
- 801 Henley, B. J. (2017). Pacific decadal climate variability: Indices, patterns and  
802 tropical-extratropical interactions. *Global and Planetary Change*, *155*(October  
803 2016), 42–55. DOI: 10.1016/j.gloplacha.2017.06.004

- 804 Hidalgo, H. G., Piechota, T. C., & Dracup, J. A. (2000, nov). Alternative principal  
805 components regression procedures for dendrohydrologic reconstructions. *Water*  
806 *Resources Research*, *36*(11), 3241–3249. DOI: 10.1029/2000WR900097
- 807 Hinkley, D. (1977). On Quick Choice of Power Transformation. *Applied Statistics*,  
808 *26*(1), 67. DOI: 10.2307/2346869
- 809 Ho, M., Lall, U., & Cook, E. R. (2016, jul). Can a paleodrought record be used to  
810 reconstruct streamflow?: A case study for the Missouri River Basin. *Water Re-*  
811 *sources Research*, *52*(7), 5195–5212. DOI: 10.1002/2015WR018444
- 812 Ho, M., Lall, U., Sun, X., & Cook, E. R. (2017, apr). Multiscale temporal variability  
813 and regional patterns in 555 years of conterminous U.S. streamflow. *Water Re-*  
814 *sources Research*, *53*(4), 3047–3066. DOI: 10.1002/2016WR019632
- 815 Huang, B., Thorne, P. W., Banzon, V. F., Boyer, T., Chepurin, G., Lawrimore,  
816 J. H., ... Zhang, H.-M. (2017, oct). Extended Reconstructed Sea Surface Tem-  
817 perature, Version 5 (ERSSTv5): Upgrades, Validations, and Intercomparisons.  
818 *Journal of Climate*, *30*(20), 8179–8205. DOI: 10.1175/JCLI-D-16-0836.1
- 819 Knoben, W. J. M., Freer, J. E., & Woods, R. A. (2019, oct). Technical note: In-  
820 herent benchmark or not? Comparing NashSutcliffe and KlingGupta efficiency  
821 scores. *Hydrology and Earth System Sciences*, *23*(10), 4323–4331. DOI:  
822 10.5194/hess-23-4323-2019
- 823 Knoben, W. J. M., Woods, R. A., & Freer, J. E. (2018). A Quantitative Hydrolog-  
824 ical Climate Classification Evaluated with Independent Streamflow Data. *Wa-*  
825 *ter Resources Research*, *54*(7), 5088–5109. DOI: 10.1029/2018WR022913
- 826 Koller, D., & Friedman, N. (2009). *Probabilistic Graphical Mod-*  
827 *els: Principles and Techniques*. MIT Press. Retrieved from  
828 <https://books.google.com.sg/books?id=7dzpHCHzNQ4C>
- 829 Krishna Kumar, K., Rajagopalan, B., & Cane, M. A. (1999, jun). On the Weaken-  
830 ing Relationship Between the Indian Monsoon and ENSO. *Science*, *284*(5423),  
831 2156–2159. DOI: 10.1126/science.284.5423.2156
- 832 Lara, A., Bahamondez, A., González-Reyes, A., Muñoz, A. A., Cuq, E., & Ruiz-  
833 Gómez, C. (2015). Reconstructing streamflow variation of the Baker River  
834 from tree-rings in Northern Patagonia since 1765. *Journal of Hydrology*,  
835 *529*(P2), 511–523. DOI: 10.1016/j.jhydrol.2014.12.007
- 836 Lavigne, F., Degeai, J. P., Komorowski, J. C., Guillet, S., Robert, V., Lahitte, P.,  
837 ... De Belizal, E. (2013). Source of the great A.D. 1257 mystery eruption  
838 unveiled, Samalas volcano, Rinjani Volcanic Complex, Indonesia. *Proceedings*  
839 *of the National Academy of Sciences of the United States of America*, *110*(42),  
840 16742–16747. DOI: 10.1073/pnas.1307520110
- 841 Lehner, B., & Grill, G. (2013, jul). Global river hydrography and network routing:  
842 baseline data and new approaches to study the world’s large river systems. *Hy-*  
843 *drological Processes*, *27*(15), 2171–2186. DOI: 10.1002/hyp.9740
- 844 Lehner, B., Liermann, C. R., Revenga, C., Vörösmarty, C., Fekete, B., Crouzet, P.,  
845 ... Wissler, D. (2011, nov). Highresolution mapping of the world’s reservoirs  
846 and dams for sustainable riverflow management. *Frontiers in Ecology and the*  
847 *Environment*, *9*(9), 494–502. DOI: 10.1890/100125

- 848 Li, J., Shao, X., Qin, N., & Li, Y. (2018, may). Runoff variations at the source of  
 849 the Yangtze River over the past 639 years based on tree-ring data. *Climate Re-*  
 850 *search*, *75*(2), 131–142. DOI: 10.3354/cr01510
- 851 Li, J., Xie, S.-P., Cook, E. R., Chen, F., Shi, J., Zhang, D. D., . . . Zhao, Y. (2019,  
 852 jan). Deciphering Human Contributions to Yellow River Flow Reductions and  
 853 Downstream Drying Using Centuries-Long Tree Ring Records. *Geophysical Re-*  
 854 *search Letters*, *46*(2), 898–905. DOI: 10.1029/2018GL081090
- 855 Libisch-Lehner, C. P., Nguyen, H. T. T., Taormina, R., Nachtnebel, H. P., & Galelli,  
 856 S. (2019, apr). On the Value of ENSO State for Urban Water Supply Sys-  
 857 tem Operators: Opportunities, TradeOffs, and Challenges. *Water Resources*  
 858 *Research*, *55*(4), 2856–2875. DOI: 10.1029/2018WR023622
- 859 Lieberman, V., & Buckley, B. (2012). *The impact of climate on South-*  
 860 *east Asia, circa 950-1820: New findings* (Vol. 46) (No. 5). DOI:  
 861 10.1017/S0026749X12000091
- 862 Liu, Y., Sun, J., Song, H., Cai, Q., Bao, G., & Li, X. (2010, may). Tree-  
 863 ring hydrologic reconstructions for the Heihe River watershed, west-  
 864 ern China since AD 1430. *Water Research*, *44*(9), 2781–2792. DOI:  
 865 10.1016/J.WATRES.2010.02.013
- 866 Lustig, T., & Pottier, C. (2007). *The Angkorian Hydraulic City: Exploitation or*  
 867 *Over-Exploitation of the Soil? Translation into English of Groslier , B-P . Le*  
 868 *cit  hydraulique angkoriennne: exploitation ou surexploitation du sol?* (As anie  
 869 20 ed.; F. Lagirarde, Ed.). Bangkok: EFEO Diffusion, As anie Bangkok.
- 870 Mantua, N. J., & Hare, S. R. (2002). The Pacific Decadal Oscillation. *Journal of*  
 871 *Oceanography*, *58*(1), 35–44. DOI: 10.1023/A:1015820616384
- 872 Marvel, K., Cook, B. I., Bonfils, C. J. W., Durack, P. J., Smerdon, J. E., &  
 873 Williams, A. P. (2019). Twentieth-century hydroclimate changes  
 874 consistent with human influence. *Nature*, *569*(7754), 59–65. DOI:  
 875 10.1038/s41586-019-1149-8
- 876 McPhaden, M. J., Zebiak, S. E., & Glantz, M. H. (2006, dec). ENSO as an In-  
 877 tegrating Concept in Earth Science. *Science*, *314*(5806), 1740–1745. DOI:  
 878 10.1126/science.1132588
- 879 Morales, M. S., Cook, E. R., Barichivich, J., Christie, D. A., Villalba, R., LeQuesne,  
 880 C., . . . Boninsegna, J. A. (2020, jul). Six hundred years of South American  
 881 tree rings reveal an increase in severe hydroclimatic events since mid-20th  
 882 century. *Proceedings of the National Academy of Sciences*, 202002411. DOI:  
 883 10.1073/pnas.2002411117
- 884 Mosteller, F., & Tukey, J. W. (1977). *Data Analysis and Regression: a second course*  
 885 *in statistics*. Addison-Wesley.
- 886 Nash, J. E., & Sutcliffe, J. V. (1970, apr). River flow forecasting through concep-  
 887 tual models part I A discussion of principles. *Journal of Hydrology*, *10*(3),  
 888 282–290. DOI: 10.1016/0022-1694(70)90255-6
- 889 Nguyen, H. T. T. (2020). *ldsr: Linear Dynamical System Reconstruction*. Retrieved  
 890 from <https://cran.r-project.org/package=ldsr>
- 891 Nguyen, H. T. T., & Galelli, S. (2018, mar). A Linear Dynamical Systems Ap-

- 892       proach to Streamflow Reconstruction Reveals History of Regime Shifts in  
893       Northern Thailand. *Water Resources Research*, 54(3), 2057–2077. DOI:  
894       10.1002/2017WR022114
- 895 Palmer, J. G., Cook, E. R., Turney, C. S. M., Allen, K. J., Fenwick, P., Cook, B. I.,  
896       ... Baker, P. (2015, dec). Drought variability in the eastern Australia and  
897       New Zealand summer drought atlas (ANZDA, CE 15002012) modulated by  
898       the Interdecadal Pacific Oscillation. *Environmental Research Letters*, 10(12),  
899       124002. DOI: 10.1088/1748-9326/10/12/124002
- 900 Palmer, W. C. (1965). *Meteorological Drought. Research Paper No. 45*. U.S. Depart-  
901       ment of Commerce Weather Bureau.
- 902 Panyushkina, I. P., Meko, D. M., Macklin, M. G., Toonen, W. H. J., Mukhamadiev,  
903       N. S., Konovalov, V. G., ... Sagitov, A. O. (2018, oct). Runoff variations in  
904       Lake Balkhash Basin, Central Asia, 17792015, inferred from tree rings. *Climate*  
905       *Dynamics*, 51(7-8), 3161–3177. DOI: 10.1007/s00382-018-4072-z
- 906 Pederson, N., Hessel, A. E., Baatarbileg, N., Anchukaitis, K. J., & Di Cosmo, N.  
907       (2014). Pluvials, droughts, the Mongol Empire, and modern Mongolia. *Pro-*  
908       *ceedings of the National Academy of Sciences of the United States of America*,  
909       111(12), 4375–4379. DOI: 10.1073/pnas.1318677111
- 910 Pederson, N., Leland, C., Nachin, B., Hessel, A. E., Bell, A. R., Martin-Benito, D.,  
911       ... Davi, N. K. (2013). Three centuries of shifting hydroclimatic regimes  
912       across the Mongolian Breadbasket. *Agricultural and Forest Meteorology*, 178-  
913       179, 10–20. DOI: 10.1016/j.agrformet.2012.07.003
- 914 Pelletier, J. D., & Turcotte, D. L. (1997). Long-range persistence in climato-  
915       logical and hydrological time series: Analysis, modeling and application to  
916       drought hazard assessment. *Journal of Hydrology*, 203(1-4), 198–208. DOI:  
917       10.1016/S0022-1694(97)00102-9
- 918 Prairie, J., Nowak, K., Rajagopalan, B., Lall, U., & Fulp, T. (2008). A stochastic  
919       nonparametric approach for streamflow generation combining observational  
920       and paleoreconstructed data. *Water Resources Research*, 44(6), 1–11. DOI:  
921       10.1029/2007WR006684
- 922 R Core Team. (2019). *R: A Language and Environment for Statistical Computing*.  
923       Vienna, Austria. Retrieved from <https://www.r-project.org/>
- 924 Rao, M. P., Cook, E. R., Cook, B. I., Palmer, J. G., Uriarte, M., Devineni, N., ...  
925       Wahab, M. (2018, aug). Six Centuries of Upper Indus Basin Streamflow Vari-  
926       ability and Its Climatic Drivers. *Water Resources Research*, 54(8), 5687–5701.  
927       DOI: 10.1029/2018WR023080
- 928 Robeson, S. M., Maxwell, J. T., & Ficklin, D. L. (2020). Bias Correction of  
929       Paleoclimatic Reconstructions: A New Look at 1,200+ Years of Upper  
930       Colorado River Flow. *Geophysical Research Letters*, 47(1), 1–12. DOI:  
931       10.1029/2019GL086689
- 932 Saji, N. H., Goswami, B. N., Vinayachandran, P. N., & Yamagata, T. (1999, sep). A  
933       dipole mode in the tropical Indian Ocean. *Nature*, 401(6751), 360–363. DOI:  
934       10.1038/43854
- 935 Satoh, Y., Kahil, T., Byers, E., Burek, P., Fischer, G., Tramberend, S., ... Wada,

- 936 Y. (2017, jul). Multi-model and multi-scenario assessments of Asian water  
 937 futures: The Water Futures and Solutions (WFaS) initiative. *Earth's Future*,  
 938 5(7), 823–852. DOI: 10.1002/2016EF000503
- 939 Sauchyn, D., & Ilich, N. (2017, nov). Nine Hundred Years of Weekly Streamflows:  
 940 Stochastic Downscaling of Ensemble Tree-Ring Reconstructions. *Water Re-*  
 941 *sources Research*, 1–18. DOI: 10.1002/2017WR021585
- 942 Sauchyn, D., Vanstone, J., St. Jacques, J.-M., & Sauchyn, R. (2015, oct).  
 943 Dendrohydrology in Canada's western interior and applications to wa-  
 944 ter resource management. *Journal of Hydrology*, 529, 548–558. DOI:  
 945 10.1016/j.jhydrol.2014.11.049
- 946 Shakun, J. D., & Shaman, J. (2009, oct). Tropical origins of North and South Pa-  
 947 cific decadal variability. *Geophysical Research Letters*, 36(19), L19711. DOI:  
 948 10.1029/2009GL040313
- 949 Sigl, M., Winstrup, M., McConnell, J. R., Welten, K. C., Plunkett, G., Ludlow,  
 950 F., ... Woodruff, T. E. (2015). Timing and climate forcing of volcanic  
 951 eruptions for the past 2,500 years. *Nature*, 523(7562), 543–549. DOI:  
 952 10.1038/nature14565
- 953 Singhrattna, N., Rajagopalan, B., Krishna Kumar, K., & Clark, M. P. (2005). Inter-  
 954 annual and interdecadal variability of Thailand summer monsoon season. *Jour-*  
 955 *nal of Climate*, 18(11), 1697–1708. DOI: 10.1175/JCLI3364.1
- 956 Sinha, A., Berkelhammer, M., Stott, L., Mudelsee, M., Cheng, H., & Biswas, J.  
 957 (2011, aug). The leading mode of Indian Summer Monsoon precipitation  
 958 variability during the last millennium. *Geophysical Research Letters*, 38(15).  
 959 DOI: 10.1029/2011GL047713
- 960 Sinha, A., Cannariato, K. G., Stott, L. D., Cheng, H., Edwards, R. L., Yadava,  
 961 M. G., ... Singh, I. B. (2007, aug). A 900-year (600 to 1500 A.D.) record  
 962 of the Indian summer monsoon precipitation from the core monsoon zone of  
 963 India. *Geophysical Research Letters*, 34(16). DOI: 10.1029/2007GL030431
- 964 Stagge, J. H., Rosenberg, D. E., DeRose, R. J., & Rittenour, T. M. (2018). Monthly  
 965 paleostreamflow reconstruction from annual tree-ring chronologies. *Journal of*  
 966 *Hydrology*, 557, 791–804. DOI: 10.1016/j.jhydrol.2017.12.057
- 967 Stahle, D. W., Cook, E. R., Burnette, D. J., Villanueva, J., Cerano, J., Burns, J. N.,  
 968 ... Howard, I. M. (2016, oct). The Mexican Drought Atlas: Tree-ring re-  
 969 constructions of the soil moisture balance during the late pre-Hispanic, colo-  
 970 nial, and modern eras. *Quaternary Science Reviews*, 149, 34–60. DOI:  
 971 10.1016/j.quascirev.2016.06.018
- 972 Stockton, C., & Jacoby, G. C. (1976). *Long-term Surface-water Supply and Stream-*  
 973 *flow Trends in the Upper Colorado River Basin Based on Tree-ring Analyses*  
 974 (Tech. Rep.). Lake Powell Research Project.
- 975 Stothers, R. B. (1984, jun). The Great Tambora Eruption in 1815 and Its After-  
 976 math. *Science*, 224(4654), 1191–1198. DOI: 10.1126/science.224.4654.1191
- 977 Strange, B. M., Maxwell, J. T., Robeson, S. M., Harley, G. L., Therrell, M. D., &  
 978 Ficklin, D. L. (2019, jun). Comparing three approaches to reconstructing  
 979 streamflow using tree rings in the Wabash River basin in the Midwestern, US.

- 980 *Journal of Hydrology*, 573, 829–840. DOI: 10.1016/j.jhydrol.2019.03.057
- 981 Tozer, C. R., Kiem, A. S., Vance, T. R., Roberts, J. L., Curran, M. A. J., & Moy,  
982 A. D. (2018). Reconstructing pre-instrumental streamflow in Eastern Australia  
983 using a water balance approach. *Journal of Hydrology*, 558, 632–646. DOI:  
984 S0022169418300738
- 985 Turner, S. W. D., & Galelli, S. (2016, may). Regime-shifting streamflow processes:  
986 Implications for water supply reservoir operations. *Water Resources Research*,  
987 52(5), 3984–4002. DOI: 10.1002/2015WR017913
- 988 Ummenhofer, C. C., Biastoch, A., & Böning, C. W. (2017). Multidecadal indian  
989 ocean variability linked to the pacific and implications for preconditioning  
990 indian ocean dipole events. *Journal of Climate*, 30(5), 1739–1751. DOI:  
991 10.1175/JCLI-D-16-0200.1
- 992 Ummenhofer, C. C., D’Arrigo, R. D., Anchukaitis, K. J., Buckley, B. M., & Cook,  
993 E. R. (2013, mar). Links between Indo-Pacific climate variability and drought  
994 in the Monsoon Asia Drought Atlas. *Climate Dynamics*, 40(5-6), 1319–1334.  
995 DOI: 10.1007/s00382-012-1458-1
- 996 van der Schrier, G., Barichivich, J., Briffa, K. R., & Jones, P. D. (2013, may).  
997 A scPDSI-based global data set of dry and wet spells for 1901-2009. *Jour-*  
998 *nal of Geophysical Research: Atmospheres*, 118(10), 4025–4048. DOI:  
999 10.1002/jgrd.50355
- 1000 Wang, J. K., Johnson, K. R., Borsato, A., Amaya, D. J., Griffiths, M. L., Henderson,  
1001 G. M., . . . Mason, A. (2019). Hydroclimatic variability in Southeast Asia over  
1002 the past two millennia. *Earth and Planetary Science Letters*, 525, 115737.  
1003 DOI: 10.1016/j.epsl.2019.115737
- 1004 Wang, Y., Byers, E., Parkinson, S., Wanders, N., Wada, Y., Mao, J., & Bielicki,  
1005 J. M. (2019, oct). Vulnerability of existing and planned coal-fired power  
1006 plants in Developing Asia to changes in climate and water resources. *Energy &*  
1007 *Environmental Science*, 12(10), 3164–3181. DOI: 10.1039/C9EE02058F
- 1008 Wells, N., Goddard, S., & Hayes, M. J. (2004, jun). A Self-Calibrating Palmer  
1009 Drought Severity Index. *Journal of Climate*, 17(12), 2335–2351. DOI:  
1010 10.1175/1520-0442(2004)017<2335:ASPDSI>2.0.CO;2
- 1011 Woodhouse, C. A., Gray, S. T., & Meko, D. M. (2006). Updated streamflow re-  
1012 constructions for the Upper Colorado River Basin. *Water Resources Research*,  
1013 42(5), 1–16. DOI: 10.1029/2005WR004455
- 1014 Xu, C., Buckley, B. M., Promchote, P., Wang, S. S., Pumijumnong, N., An, W.,  
1015 . . . Guo, Z. (2019). Increased Variability of Thailand’s Chao Phraya River  
1016 Peak Season Flow and Its Association With ENSO Variability: Evidence From  
1017 Tree Ring  $\delta 18\text{O}$ . *Geophysical Research Letters*, 46(9), 4863–4872. DOI:  
1018 10.1029/2018GL081458
- 1019 Xu, C., Pumijumnong, N., Nakatsuka, T., Sano, M., & Li, Z. (2015). A tree-ring  
1020 cellulose  $\delta 18\text{O}$ -based July-October precipitation reconstruction since AD  
1021 1828, northwest Thailand. *Journal of Hydrology*, 529(P2), 433–441. DOI:  
1022 10.1016/j.jhydrol.2015.02.037
- 1023 Yang, B., Chen, X., He, Y., Wang, J., & Lai, C. (2019). Reconstruction of

- 1024 annual runoff since CE 1557 using tree-ring chronologies in the upper  
1025 Lancang-Mekong River basin. *Journal of Hydrology*, 569, 771–781. DOI:  
1026 10.1016/j.jhydrol.2018.12.034
- 1027 Yang, B., Qin, C., Shi, F., & Sonechkin, D. M. (2012). Tree ring-based annual  
1028 streamflow reconstruction for the Heihe River in arid northwestern China from  
1029 ad 575 and its implications for water resource management. *Holocene*, 22(7),  
1030 773–784. DOI: 10.1177/0959683611430411
- 1031 Yu, E., King, M. P., Sobolowski, S., Otterå, O. H., & Gao, Y. (2018, jun). Asian  
1032 droughts in the last millennium: a search for robust impacts of Pacific Ocean  
1033 surface temperature variabilities. *Climate Dynamics*, 50(11-12), 4671–4689.  
1034 DOI: 10.1007/s00382-017-3897-1
- 1035 Yuan, Y., Shao, X., Wei, W., Yu, S., Gong, Y., & Trouet, V. (2007, dec). The  
1036 Potential to Reconstruct Manasi River Streamflow in the Northern Tien  
1037 Shan Mountains (NW China). *Tree-Ring Research*, 63(2), 81–93. DOI:  
1038 10.3959/1536-1098-63.2.81
- 1039 Zhang, D., Zhang, Q., Werner, A. D., & Liu, X. (2016). GRACE-Based Hydrological  
1040 Drought Evaluation of the Yangtze River Basin, China. *Journal of Hydrometeo-*  
1041 *rology*, 17(3), 811–828. DOI: 10.1175/JHM-D-15-0084.1
- 1042 Zhang, T., Yuan, Y., Chen, F., Yu, S., Zhang, R., Qin, L., & Jiang, S. (2018, feb).  
1043 Reconstruction of hydrological changes based on tree-ring data of the Haba  
1044 River, northwestern China. *Journal of Arid Land*, 10(1), 53–67. DOI:  
1045 10.1007/s40333-017-0034-2